

**DEVELOPMENT OF A NUMERICAL MODEL FOR BLOOD RHEOLOGY
SUBJECTED TO PULSATING POISEUILLE FLOW IN A CYLINDRICAL
VESSEL**

by

Tim Van de Vyver

A thesis submitted to the Faculty of the University of Delaware in partial fulfillment of the requirements for the degree of Master of Science in Chemical Engineering

Spring 2019

© 2019 Tim Van de Vyver
All Rights Reserved

**DEVELOPMENT OF A NUMERICAL MODEL FOR BLOOD RHEOLOGY
SUBJECTED TO PULSATING POISEUILLE FLOW IN A CYLINDRICAL
VESSEL**

by

Tim Van de Vyver

Approved: _____
Norman J. Wagner, Ph.D
Professor in charge of thesis on behalf of Advisory Committee

Approved: _____
Antony N. Beris, Ph.D
Professor in charge of thesis on behalf of Advisory Committee

Approved: _____
Eric M. Furst, Ph.D
Chair of the Department of Chemical and Biomolecular Engineering

Approved: _____
Levi T. Thompson, Ph.D
Dean of the College of Engineering

Approved: _____
Douglas J. Doren, Ph.D.
Interim Vice Provost for Graduate and Professional Education

ACKNOWLEDGMENTS

First I would like to thank professor Antony N. Beris for guiding me through this project and for the chance to learn for his outstanding mathematical knowledge. I would also like to thank professor Wagner for accepting me in to his group an giving me all the necessary support, materials and guiding during this exchange program. I wish to thank him and Ilse Smets as well for accepting me into the Dual Degree program and giving me the opportunity to expand my horizons abroad.

Most importantly, I wish to express my gratitude to the most friendly, open, positive minded and supportive people I have ever met: Mark Casagrande and Alex Tunnell. This year would not have been possible without them and I like to thank them for taking me into their home as family. I am also most thankful for Ann Vanhaverbeke, Tom Van de Vyver, Geert Van de Vyver and Jolien Helmer for always being there for me wherever I go and supporting me no matter what. Special thanks also goes to Tomas Van Ryckeghem, Alix-Anne Schreinemacher and Kasper Verhulst.

TABLE OF CONTENTS

LIST OF TABLES	vi
LIST OF FIGURES	vii
LIST OF SYMBOLS AND ABBREVIATIONS	xiii
ABSTRACT	xiv
 Chapter	
1 INTRODUCTION	1
1.1 Motivation and Background	1
1.2 Goal and Objectives	9
1.3 Blood Modelling	10
1.3.1 General Newtonian Fluid	12
1.3.2 Viscoelastic Models	15
1.3.3 Thixotropic Models	16
1.3.4 UD-LAOS Flow	21
2 PROBLEM DESCRIPTION AND METHODS	24
2.1 Problem Description	24
2.2 Methods	26
2.2.1 Output Variable Formulation	26
2.2.2 Making the Problem Dimensionless	28
2.2.3 Solving the Equations	30
2.3 Figure Representation in the Results Section	32
3 RESULTS AND DISCUSSION	34
3.1 Method Validation	34
3.1.1 Newtonian Fluid	34

3.1.2	Elastic Solid	39
3.1.3	Maxwell Fluid	43
3.1.4	Power Law Model	47
3.1.5	Carreau Model	51
3.2	Modified Stephanou model	53
3.2.1	Structural parameter	54
3.2.2	Collocation Method for modified Stephanou model	58
4	CONCLUSIONS AND FUTURE WORK	65
	BIBLIOGRAPHY	67
	Appendix	
A	REPRINT PERMISSION LETTERS	70
B	ELASTIC LIMIT OF THE MAXWELL FLUID	73
C	TABLES	75
D	MATLAB CODE	79
E	SOFTWARE LICENSE FILES	93

LIST OF TABLES

2.1	Examples of dimensionless numbers in a tubular vessel for fully developed axially pulsating Poiseuille flow.	29
3.1	Physical parameters used in result section for a Newtonian fluid. . .	34
3.2	Physical parameters used in result section for an elastic solid. . . .	40
3.3	Physical parameters used in result section for a Maxwell fluid. . . .	43
3.4	Physical parameters used in result section for a power law model. . .	47
3.5	Physical parameters used in result section for a Carreau model. . . .	51
3.6	Physical parameters used in result section for the modified Stephanou model.	54
C.1	Structural parameter node coefficients	76
C.2	Z node coefficients	77
C.3	σ_{rz} node coefficients	78

LIST OF FIGURES

1.1	Schematic picture of red blood cells, white blood cells and blood platelets in an artery.	1
1.2	Schematic depiction of shear of a fluid element.	3
1.3	Schematic picture of the interconnection between modelling and experiments.	4
1.4	Depiction of rouleaux formation of red blood cells	5
1.5	Cross section of blood vessel showing the formation of a RBC depletion layer when blood flows.	7
1.6	Most commonly used generalized Newtonian models.	13
1.7	Logarithmic plot of the viscosity versus the shear rate for a shear thinning fluid according to the Carreau model.	14
1.8	2-dimensional projections of the shear stress versus the strain for different frequencies	22
2.1	Schematic picture of the system geometry and flow conditions. . .	25
2.2	Quadratic bilinear coordinate transformation according to equation 2.14 with $r_b^2 = 0.1$	31
2.3	Schematic depiction of output variable representation.	33
3.1	Newtonian axial velocity for pulsatile flow for $r = R$ (upper curve) and $r = R/2$ (lower curve) versus the time in SI-units.	36
3.2	Newtonian axial velocity for pulsatile flow for 5 equidistant time points in the periodic domain in SI-units.	36

3.3	Newtonian shear rate for pulsatile flow for 5 equidistant time points in the periodic domain in SI-units.	37
3.4	Newtonian shear stress for pulsatile flow for 5 equidistant time points in the periodic domain in SI-units.	37
3.5	Error comparison for pulsatile flow between the collocation method and a second order finite difference method for the same number of equations that need to be solved.	38
3.6	2D projection of the Lissajous plot in the shear stress-shear rate domain for pulsatile flow for a Newtonian fluid.	39
3.7	Axial velocity for oscillatory flow for an elastic solid for 5 equidistant time points in the periodic domain in SI-units.	41
3.8	Shear rate for oscillatory flow for an elastic solid for 5 equidistant time points in the periodic domain in SI-units.	42
3.9	Shear stress for oscillatory flow for an elastic solid for 5 equidistant time points in the periodic domain in SI-units.	42
3.10	2D projection of the Lissajous plot in the shear stress-shear rate domain for oscillatory flow for an elastic solid.	43
3.11	Absolute error for pulsatile flow for a Maxwell fluid with the collocation method, and $\tilde{t}_m = 0.2$	44
3.12	Axial velocity profile for a Maxwell fluid subjected to pulsatile flow for 5 equidistant time points in SI-units.	45
3.13	Dimensionless shear rate profile for a Maxwell fluid subjected to pulsatile flow for 5 equidistant time points in SI-units.	45
3.14	Dimensionless shear stress profile for a Maxwell fluid subjected to pulsatile flow for 5 equidistant time points in SI-units.	46
3.15	2D projection of the Lissajous plot in the shear stress-shear rate domain for a Maxwell fluid subjected to pulsatile flow.	47
3.16	Dimensionless axial velocity profile for a power law fluid in steady state flow for $q = 0.2$	48

3.17	Absolute error of the collocation method in function of the number of unknowns for a power law fluid in steady state flow for $q = 0.01$.	49
3.18	Dimensionless axial velocity profile for a power law fluid in steady state flow for $q = 0.01$.	50
3.19	Absolute error of the collocation method in function of the number of unknowns for a power law fluid in steady state flow for $q = 0.01$.	50
3.20	Transient dimensionless velocity profile for a Carreau fluid subjected with $q = 0.1$ and $Wi = De = 10$ for oscillating flow.	52
3.21	Transient shear rate profile for a Carreau fluid with $q = 0.1$ and $Wi = De = 10$ for oscillating flow.	53
3.22	Radial profiles of the structure parameter for the modified Stephanou model subjected to pulsatile flow at 5 equidistant points in a period for $t_\lambda = 50, t_a = 0, t_b = 0.5, Wo = 0.23$ and $\frac{d\tilde{p}}{d\tilde{z}} = -7.9$.	55
3.23	Radial profiles of the structure parameter for the modified Stephanou model subjected to pulsatile flow at 5 equidistant points in a period for $t_\lambda = 10, t_a = 0, t_b = 0.5, Wo = 0.23$ and $\frac{d\tilde{p}}{d\tilde{z}} = -7.9$.	56
3.24	Radial profiles of the structure parameter for the modified Stephanou model subjected to pulsatile flow at 5 equidistant points in a period for $t_\lambda = 50, t_a = 0, t_b = 0.25, Wo = 0.23$ and $\frac{d\tilde{p}}{d\tilde{z}} = -7.9$.	57
3.25	Radial profiles of the structure parameter for the modified Stephanou model subjected to pulsatile flow at 5 equidistant points in a period for $t_\lambda = 50, t_a = 5, t_b = 0.5, Wo = 0.23$ and $\frac{d\tilde{p}}{d\tilde{z}} = -7.9$.	58
3.26	Lissajous plot in the shear stress - shear rate domain for the viscoelastic part of the modified Stephanou model subjected to pulsatile flow for $t_\lambda = 50, t_a = 0, t_b = 0.5, G = 0.019$ and $\frac{d\tilde{p}}{d\tilde{z}} = -7.9$.	60
3.27	Shear rate for 5 equidistant time points in the periodic domain for the viscoelastic part of the modified Stephanou model subjected to pulsatile flow for $t_\lambda = 50, t_a = 0, t_b = 0.5, G = 0.019$ and $\frac{d\tilde{p}}{d\tilde{z}} = -7.9$.	61
3.28	Shear rate for $r = R$ and $r = 0.95R$ for the viscoelastic part of the modified Stephanou model subjected to pulsatile flow for $t_\lambda = 50, t_a = 0, t_b = 0.5, G = 0.019$ and $\frac{d\tilde{p}}{d\tilde{z}} = -7.9$.	62

- 3.29 Shear stress for 5 equidistant time points in the periodic domain for the viscoelastic part of the modified Stephanou model subjected to pulsatile flow for $t_\lambda = 50, t_a = 0, t_b = 0.5, G = 0.019$ and $\frac{d\bar{p}}{d\bar{z}} = -7.9$. 63
- 3.30 Axial velocity for 5 equidistant time points in the periodic domain for the viscoelastic part of the modified Stephanou model subjected to pulsatile flow for $t_\lambda = 50, t_a = 0, t_b = 0.5, G = 0.019$ and $\frac{d\bar{p}}{d\bar{z}} = -7.9$ 64

LIST OF SYMBOLS AND ABBREVIATIONS

Subscripts		e	Elastic
0	Low shear rates	\max	Maximum value
γ	Yield limit	p	Plastic
∞	High shear rates	Notation	
λ	Structural term	\hat{a}	Upper convected derivative
b	Blood Plasma	$ a $	Absolute value
C	Conformation or viscoelastic part	\mathbf{A}	Matrix
c	Carreau model	∇	Derivative with respect to space
$crit$	Critical value	∇^2	Laplace operator
f	Fibrinogen	∂	Partial derivative operator
i, j	Numbering	\tilde{a}	Dimensionless value
R	Thixotropic part	$\underline{\underline{a}}$	Third-order tensor
r	Reference state	\underline{a}	Second-order tensor
s	Solvent	\underline{a}	Vector
SS	Steady state	a^T	Transpose
w	At the wall	D	Material Derivative operator
z	in the axial direction		

d	Derivative operator	De	Deborah number
t_*	Time constant	E	Absolute error
Symbols		G	Elastic modulus [Pa]
$\dot{\gamma}$	Shear rate [1/s]	g	Gravitational Constant [m/s ²]
ϵ	Amplitude [-]	Hct	Hematocrit [-]
η	Viscosity [Pa s]	I	First Invariant of tensor
$\frac{\partial p}{\partial z}$	Axial pressure gradient [Pa/m]	i	Complex number
γ	Strain or shear [-]	J_0	Bessel function of order 0
λ	Structural parameter [-]	K	Power law constant
ω	Angular velocity [1/s]	k	Kinetic constant
ρ	Density [kg/m ³]	m	Number of Chebyshev nodes
σ	Shear stress [Pa]	n	Number of harmonics
$\underline{\underline{\tilde{c}}}$	Dimensionless conformation tensor	p	Pressure [Pa]
$A(t)$	Time dependent part	q	Power law exponent
$B(r)$	Radial dependent part	R	Tube radius [m]
c	Concentration [g/dl]	r	Radial coordinate [m]
cp	Continuation parameter	s	Carreau model exponent [-]
D	Shear rate deformation [1/s]	T	Sinusoidal period [s]
		t	Time [s]
		T_m	Chebyshev Polynomial of the first kind of order m

T_e	Temperature [K]
v	Velocity [m/s]
Wi	Weissenberg number
x	Any spatial dimension [m]
y	Any output variable
z	Axial coordinate [m]
$\underline{\underline{\delta}}$	Unit tensor [-]

ABSTRACT

The overall goal of this project is to develop a robust and accurate numerical method for studying the flow of blood in arterial, pulsatile flow. The most important contribution of this work is the development of an efficient code, that is able to solve complex blood flow constitutive models. This can be a great aid in defining new rheological models more suited for pulsating Poiseuille flow in the future, coming one step closer to modelling the flow conditions in the human body. The model is meant to use in combination with a microfluidic device that acts under the same flow conditions. It can help to understand the underlying physics and to make realistic predictions for other flow parameters. Experiments with microfluidic device are needed to come up with better conditioned models and better adapted parameters for pulsating Poiseuille flow. This opens the path to a new method of researching blood rheology in a way that more closely resembles the flow conditions in the human body.

The code is designed to take advantage of the mathematical form of the flow conditions and the cylindrical geometry. The result is a collocation method, where orthogonal Fourier and Chebyshev polynomials are fitted to the solutions. This makes the solution semi-analytic and introduces only an interpolation error on top of the machine error. The model was successfully validated for the calculation of Newtonian fluids, elastic solid, Maxwellian fluids and power law fluids, whilst also showing the capability to solve more complicated models including a structural parameter. The algorithm is able to reach much higher accuracies than finite difference methods whilst solving for much less unknowns, making it also faster.

Chapter 1

INTRODUCTION

1.1 Motivation and Background

Interest in blood from physiological point of view can be traced back to Ancient Egyptian medicine or Mesopotamia [1]. It is of major interest for the diagnosis and treatment of diseases. A lot of research has been done concerning the composition of blood (Figure 1.1). A doctor takes blood tests which are analyzed in a clinical laboratory and compared to a range of standard values. But because the characteristics of blood change when it flows, the study of blood flow can be a very valuable tool to aid in the diagnosis and treatment of blood related diseases, e.g. stenosis and thrombosis. The study of blood flow is helpful for understanding and treating any disease which changes the flow properties or microstructure of the blood.

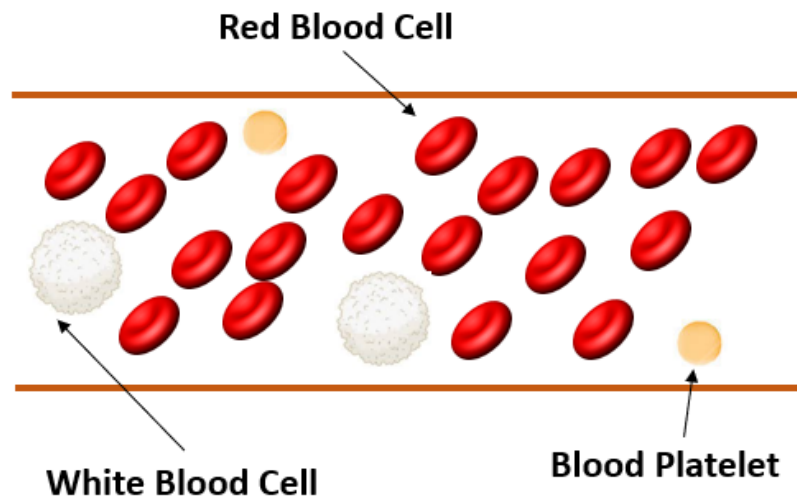


Figure 1.1: Schematic picture of red blood cells, white blood cells and blood platelets in an artery.

Rheology is the study of flow. More concrete, the field of rheology studies the relationship between velocity or momentum, shear, shear rate, applied force or pressure drop, time and geometry for a certain fluid. Figure 1.2 shows a schematic depiction of the shear of a fluid element; the shear is equal to $\Delta L/H$. For the case of blood flow in the human body, the geometry is the arterial network, which can be represented as a set of cylindrical tubes. The radius of the cylindrical tubes varies throughout the network from large arteries to small capillaries. The driving force is mainly the pulsatile pressure drop exerted by the beating heart in the larger vessels and mainly the capillary forces in the small capillaries. This driving force is opposed by the drag force between the fluid and the wall and the viscous forces within the fluid [2]. The blood vessels can expand when a force or stress is exerted on them and when the stress at the wall becomes too large they can even break. Blood flow has many important functions in the body. The main functions are transport of oxygen and nutrients, removal of waste products, transport of hormones and other messenger molecules and protecting the body against diseases. In the bloodstream many physical and chemical processes take place. These processes impact the microstructure of blood, giving rise to complex flow phenomena. This makes the study of blood flow of major interest in biology, healthcare, physics and chemistry [3].

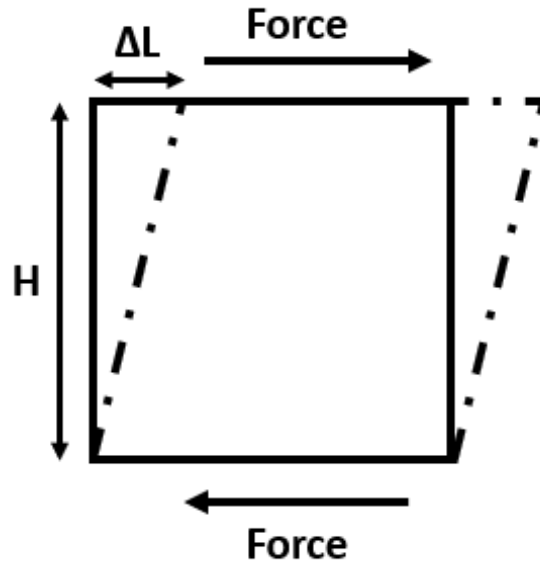


Figure 1.2: Schematic depiction of shear of a fluid element.

Modelling is a very important tool in understanding the nature of blood. By developing models of the blood flow, which are constructed using theories of Physics and Chemistry, and comparing these models with experimental data, the underlying physical and chemical mechanisms of blood flow can be derived. Once a model has been established, it can also serve to predict other blood flows. Figure 1.3 show this in a schematic way. Blood consists of a concentrated suspension of cells, about 46 %, within plasma. Plasma is an aqueous solution, approximately 90-92 % water, of various proteins (mainly albumin), electrolytes, nutrients, gases and waste products [4, 5]. More than 99 % of the cells are red blood cells (RBCs), also known as erythrocytes. They can deform under stress and have a unique disk-doughnut shape. When not deformed they have a diameter of about $7.7 \pm 0.7 \mu\text{m}$, $1.4 \pm 0.5 \mu\text{m}$ central and $2.4 \pm 0.5 \mu\text{m}$ peripheral thickness [6]. RBCs have no nucleus or cytoskeleton and can to a first approximation mechanically be viewed as a deformable capsule with an elastic membrane [7]. The volume fraction of erythrocytes is called the hematocrit and it is approximately 0.45 for healthy men and 0.42 for healthy women. The other 1 % of the cells are white blood cells, also known as

leukocytes, and platelets. White blood cells are approximately spherical in shape with a diameter ranging from 7 to $22\mu m$ and are very important for the immune system. Platelets have a rounded or oval shape with dimensions from 2 – $4\mu m$ and have the function to close and repair damage to the blood vessel walls [3].

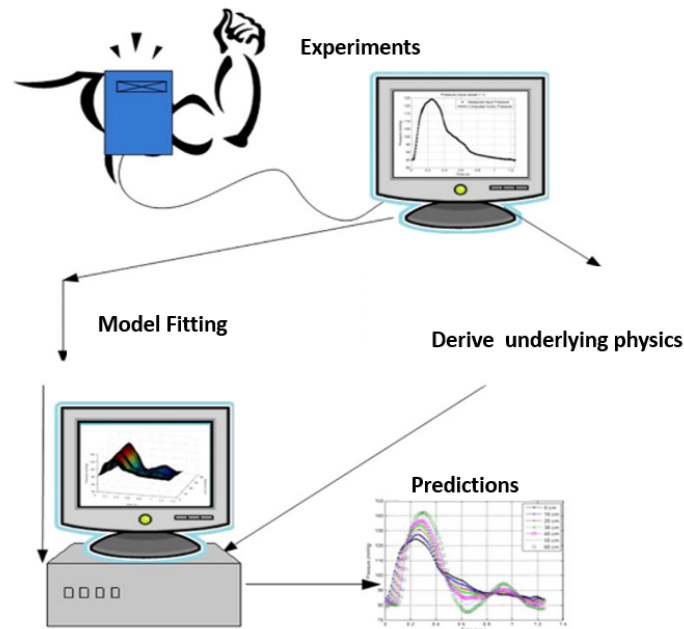


Figure 1.3: Schematic picture of the interconnection between modelling and experiments.

An important characteristic of the RBCs is their deformability which allows them to pass through narrow capillaries as small as $2.9\mu m$ diameter and to adapt to the flow field. The latter is also known as relaxation of RBCs [8]. At lower shear rates however the RBCs stack into a coin structure which is known as rouleaux (Figure 1.4) [9, 10, 11]. The main factors contributing to the extent of rouleaux formation are the hematocrit and the fibrinogen concentration. This can be explained by the fact that fibrinogen polymerizes into fibrin, the major protein component of blood clots, as part of the coagulation process. This process is similar to the formation of blood clots in case of an open wound [12].

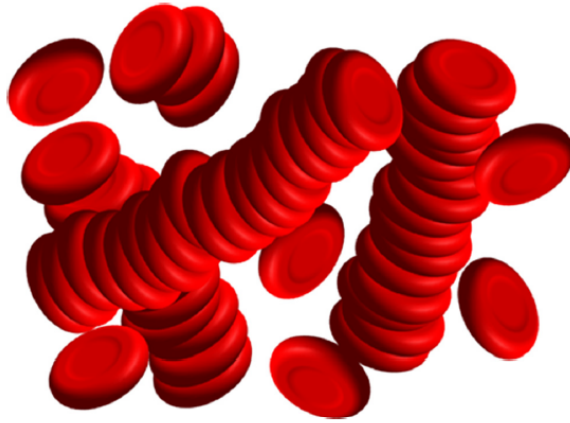


Figure 1.4: Depiction of rouleaux formation of red blood cells [13].¹

The rouleaux formation gives blood a certain strength which leads to a viscoelastic behavior [14, 15, 16]. Viscoelastic means that the fluid exhibits both viscous and elastic properties [17, 18]. Examples of purely viscous fluids are Newtonian fluids. A Newtonian fluid is an ideal fluid in which the shear stress is directly proportional to the shear rate, i.e. the more the fluid is sheared, the more stress is experienced by the fluid. The proportionality between the shear stress and the shear rate is called the viscosity and is a measure for how easily to fluid flows. The higher the viscosity, the more stress must be exerted on the fluid to reach a certain velocity. For a Newtonian fluid, the viscosity is constant, but in the case of a general Newtonian fluid, the viscosity can depend on the shear rate [2]. Blood by example is also shear thinning, which means that the viscosity decreases with increasing shear rate. The harder the blood is sheared the less additional energy it takes to reach a higher velocity. All the energy put in a viscous fluid is dissipated as heat, due to molecular motion. This deformability of the red blood cells gives rise to this shear thinning behavior of blood at high shear rate, because of a better alignment with the blood velocity stream lines which leads to a minimization of energy [13]. Most oils closely resemble the behavior of a viscous fluid, which is a reason why they

¹ Reprinted with permission from [13]. Copyright 2018, The Society of Rheology.

are often used in dashpots. Completely opposite to a viscous fluid is a purely elastic solid. All the energy put into an elastic solid is stored and released again in the same form. An elastic solid is most easily imagined as a spring. Viscoelastic solids have characteristics of both viscous fluids and elastic solids, so part of the input energy is stored, and another part is dissipated into heat. The best way to imagine this is like a spring and a dashpot in series, similar to an automatic door closer. For higher frequencies this leads to interesting phenomena like resonance. Viscoelasticity and shear thinning lead to a flow rate enhancement when subjected to pulsatile flow, meaning that blood is more easily transported throughout the body by a pulsating pressure gradient than by a constant pressure gradient [19, 20, 21]. This can be a logical explanation for why blood and the heart are designed this way by nature.

Another consequence of the microfluidic structure is thixotropy, which means that the longer the blood is in shear flow, the lower its viscosity becomes. This is because of the continuous breakdown of the rouleaux structure in time and the structuring of the red blood cells parallel to the streamlines of the flow. When the shear is lifted the blood structure returns to its original state [13]. The complex nature of blood can thus mainly be broken down into shear thinning behavior, viscoelasticity and thixotropy, resulting from the complex blood structure and deformability of the RBCs. At least when blood is considered a simple fluid, meaning that the blood cells are equally distributed and that the composition is uniform.

In reality the red blood cells migrate more towards the center of the blood vessel and the white blood cells and platelets migrate towards the edge of the blood vessel [22]. A RBC-depletion layer forms close to the wall (Figure 1.5). This leads to a lower viscosity near the boundary, which promotes blood flow. This effect is called syneresis [23]. Related to this is the Fahraeus effect, which is the migration of deformable cells to regions with a higher velocity. One reason for this concentration variation is the simple volume exclusion effect: cells can not pass through the

wall, so there is always a region near the wall with a cell volume fraction lower than the nominal value. The other reason is that RBCs and all deformable particles migrate away from walls during shear due to hydrodynamic interaction effects with the walls [24]. The syneresis effect, which creates a lower viscosity near the wall, increases when the tube diameter becomes smaller because the boundary layer becomes a relatively larger part of the blood vessel. For very small capillaries the viscosity increases again because the diameter of capillaries has become smaller than the size of the RBCs. This is called the Fahraeus-Lindqvist effect [25, 26]. At very small diameter capillary forces become dominant over pressure and inertia forces. Biologically the syneresis also makes sense because the white blood cells and red blood cells perform biological functions close to the wall and the red blood cells mainly transport oxygen throughout the body, thus benefitting from a decreased viscosity.

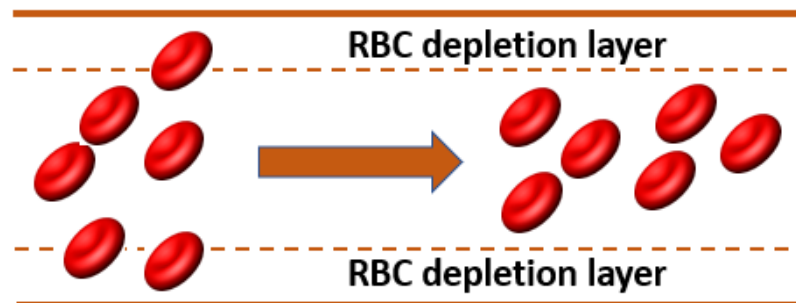


Figure 1.5: Cross section of blood vessel showing the formation of a RBC depletion layer when blood flows.

Many models that account for the shear thinning, viscoelastic and thixotropic behavior of blood have been developed (see section 1.3). These models describe a relationship between the shear stress, the shear rate and the strain. These models have been validated in shear rheometers, which measure the rheological properties under simple shear flow, i.e. with a constant shear rate throughout the entire

measurement device. The behavior of blood under steady state flow has been studied in depth and is thoroughly understood, but it is of more interest to be able to study the transient behavior of blood and more specifically the pulsatile behavior, as the heart creates a pulsating blood flow. The viscoelastic and thixotropic nature of blood is mainly relevant in transient flow. Some transient shear rheometer experiments have been performed, but the data considering transient blood flow is still not that extensive. More experiments and biological knowledge are needed to find the full dependency of rouleaux formation on the blood components. But taking measurements of blood rheology parameters in in vivo conditions is not easy, because the characteristics of blood will change with extended time from withdrawal. Also, the storage temperature plays an important role and affects the measurable time for accurate rheology measurements. Care is required when rewarming cooled blood cells to physiological temperature to not damage the cells. Evaporation, interfacial effect and sedimentation must also be taken into account, but the effect of those can be mitigated by choosing an appropriate geometry [27, 28, 29].

The flow in the arterial network however is pressure driven Poiseuille flow, which means that the shear rate varies with the radius of the blood vessel. That is why this thesis will focus on calculating the velocity profile for pulsatile Poiseuille flow. The modelling of Poiseuille flow can be combined with experimental measurements in a microfluidic channel, creating a new way of characterizing blood rheology that more closely resembles the conditions in the human body. For one specific radius (typically the wall radius), where the shear is constant, the results can be compared to the shear rheometer tests. To be able to model blood undergoing pulsatile Poiseuille flow with a more complicated rheological model whilst still retaining high accuracy, a mathematical approach is developed which differs from the common numerical methods used in commercial software packages.

1.2 Goal and Objectives

The goal of this thesis is to develop a computational code that is able to calculate the radial profile in a cylindrical vessel of a complex fluid under pulsatile flow. Specifically this will serve to model the blood flow in the arterial network. While modelling the entire blood network with realistic rheological models is a goal for future work, this thesis focuses on the basic building block of the arterial network which is a small cylindrical arterial vessel with rigid walls. Blood is a complex fluid because it is viscoelastic, shear thinning and thixotropic. Models for pure shear flow in a rheometer have been developed in previous works, e.g. The HAWB model, AAB model and the Johnson and Segalman model [13, 17, 30]. This work focuses on implementing simple shear models for Poiseuille flow by combining the previously developed relationship between shear stress and shear rate with the Cauchy momentum equation and the mass conservation equation whilst applying the no-slip condition, because syneresis is not considered in this work, and making use of the cylindrical symmetry. As future works aim to model the entire blood flow network with realistic rheological models for blood, it is important that the code for the basic building block works as computationally efficient as possible, which is why another approach which focuses on collocation using orthogonal polynomials is tested. This method shows the potential to be more accurate than the traditional finite difference and finite volume approach whilst using less computational power by making use of the specific geometry and flow conditions of the problem. For general flow problems in more complicated geometries this method is not applicable.

This goal translates into 3 objectives:

1. Validation of the computational code
2. Validating relaxation equation for structural parameter
3. Apply computational code to advanced blood rheology model

The first objective is achieved by comparing the numerical solutions with analytical

solutions for known fluid models. The cases chosen to validate the code are Newtonian fluids, elastic solids, Maxwellian fluids and power law fluids. The second objective is related to blood phenomena with respect to the blood structure: viscoelasticity, thixotropy and shear thinning. This is often represented with a structural parameter λ that goes from zero (no structure) to unity (fully structured). It is however not known whether the current relaxation equations for λ play a significant role in pulsatile Poiseuille flow and capture the right order of magnitude for these flow conditions. If objective two is confirmed, the code can be used to calculate the flow characteristics for complex blood rheology that includes a structural model parameter. Afterwards it can be investigated how sensitive the model outputs (axial velocity, strain, shear rate, shear stress and the structural parameter) are to changes in the input parameters of the model (viscosity, elastic modulus, radius, steady state pressure drop, amplitude, frequency, density and time constants). This is important because the model parameters vary depending on the blood donor. If the model is completely insensitive to the model parameters, it can not be used for diagnostic purposes. Too sensitive model parameters can however be a sign of numeric instability of the model, which makes the model not trustworthy.

1.3 Blood Modelling

The main tools to study blood rheology are laboratory experiments and computer modelling. The function of computer modelling is to recreate the laboratory experiments by introducing model parameters and equations based on physical phenomena. Thus matching the model to the experimental results creates insight in the underlying physics as well as the possibility to predict the experiments for different conditions (Figure 1.3). The first step to model the blood flow is to adopt an equation that connects the velocity or momentum with the applied force or pressure drop. This equation is a microscopic momentum balance known as the Cauchy

momentum equation:

$$\frac{D(\rho v)}{Dt} = \left(\frac{\partial(\rho v)}{\partial t} + \underline{v} \cdot \underline{\nabla} \rho v \right) = -\underline{\nabla} p + \underline{\nabla} \cdot \underline{\underline{\sigma}} - \underline{g} \quad (1.1)$$

This is a force balance in vector form that is valid at every microscopic volume element in a fixed coordinate system. The left side of the equation is the change of momentum in time, the right side are the forces that change the momentum: the pressure forces, the viscous forces that cause a stress in the fluid and the gravitational forces. Because the total mass of the system needs to remain constant, the problem must also satisfy the mass conservation equation, which is a scalar equation:

$$\frac{\partial \rho}{\partial t} + \underline{\nabla} \cdot (\rho \underline{v}) = 0 \quad (1.2)$$

Equations 1.1 and 1.2 are universally valid for all fluids. The equations are however not solvable without specifying the functional relationship between shear stress and flow kinematics. The equations for the shear rate are generally expressed in tensorial form (see section 1.3). To find an overall solution, equations 1.1 and 1.2 and the shear stress equation must be integrated with an initial condition for each time derivative and two boundary conditions for each spatial dimension. When there is no interest in finding the solution for all spatial dimensions and the time dimension the equations can be greatly simplified. This can happen when steady state is assumed or spatial symmetries are present or spatial averaging over one or multiple dimensions is applied.

The following sections will discuss common models to study blood rheology in increasing order of complexity. A lot of effort has been done to capture the rheologic phenomena of blood, resulting from the structure at a microlevel, in macroscopic models incorporating physiological parameters. The macroscopic models thus form the connection between the physiological parameters and what is happening at the microlevel. The main rheological phenomena that need to be included are viscoelasticity, shear thinning and thixotropy. As noted, syneresis is not taken

into account in this thesis and blood is treated as a homogeneous fluid. It can however be added to the model in future works.

1.3.1 General Newtonian Fluid

The general Newtonian model is given by equation 1.3 :

$$\underline{\underline{\sigma}} = 2\eta(\underline{\underline{D}})\underline{\underline{D}} \quad (1.3)$$

$$D_{i,j} = \frac{1}{2} \left(\frac{\partial v_j}{\partial x_i} + \frac{\partial v_i}{\partial x_j} \right)$$

If the fluid is only sheared in one direction, the tensorial equation reduces to a single scalar equation:

$$\sigma_{12} = \eta(|\dot{\gamma}|)\dot{\gamma} \quad (1.4)$$

The connection between $\underline{\underline{D}}$ and $\dot{\gamma}$ is formally defined as $\dot{\gamma} = \sqrt{\frac{1}{2}\underline{\underline{D}} : \underline{\underline{D}}}$. Generalized Newtonian fluids cover Newtonian fluids, shear thinning or pseudoplastic fluids and shear thickening or dilatant fluids as well as fluids with a yield stress. For a Newtonian fluid η is constant and the shear stress becomes directly proportional to the shear rate. This is observed for blood flow at high shear rates. The common explanation for this is that the high shear brakes apart all structure and makes the blood more homogeneous [13]. The Newtonian model is most commonly used in rheology and aerodynamics equations because of its simplicity. For a Newtonian fluid, the Cauchy momentum equation (1.1) reduces to the well-known Navier-stokes equation:

$$\frac{D(\rho v)}{Dt} = -\nabla p + \eta \nabla^2 v - \underline{g} \quad (1.5)$$

The viscosity of a shear thinning fluid decreases with increasing shear rate and the viscosity of a shear thickening fluid increases with increasing shear rate. Some fluids deform only elastically below a certain stress, called the yield stress. At least it seems that way when the fluid is looked at for a relatively short time scale. When waiting for millions of years even mountains flow in a viscous manner. But when the observation time of the experiment is short in comparison to the relaxation time

of the solid, a yield stress model is the best approximation of the rheology. This results in a non-zero shear stress at zero shear rate. Figure 1.6 gives an overview of the most common general Newtonian models:

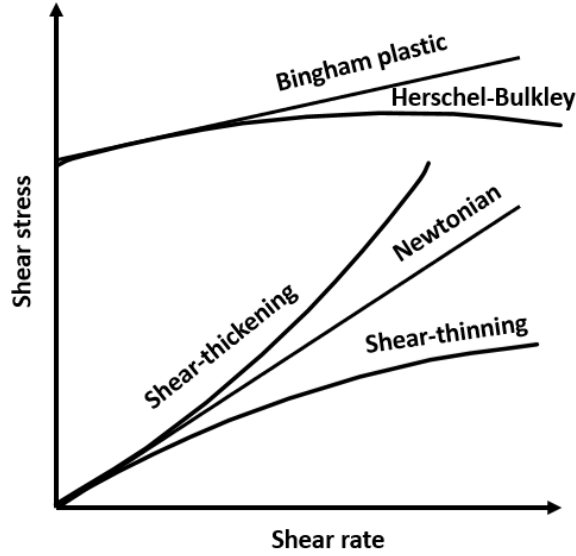


Figure 1.6: Most commonly used generalized Newtonian models.

The Casson model is often fitted to steady state blood rheology data with success. The shear stress of the Casson model is discontinuous and given by the following set of equations:

$$\sqrt{\sigma} = \begin{cases} \sqrt{\sigma_\gamma} + \sqrt{\eta|\dot{\gamma}|} & \sigma \geq \sigma_\gamma \\ 0 & \sigma < \sigma_\gamma \end{cases} \quad (1.6)$$

Apostolidis and Beris also found a relationship between the model parameters (the yield stress and viscosity) and the most important parameters in rouleaux formation (Hematocrit, critical Hematocrit, fibrinogen concentration and the temperature). This relationship is given in equations 1.7 - 1.9.

$$\sigma_\gamma = \begin{cases} (Hct - Hct_c)^2(0.5084C_f + 0.4517)^2 & Hct > Hct_{crit} \\ 0 & Hct \leq Hct_{crit} \end{cases} \quad (1.7)$$

$$Hct_{crit} = \begin{cases} 0.3126C_f^2 - 0.468C_f + 0.1764 & C_f < 0.75 \\ 0.0012 & C_f \geq 0.75 \end{cases} \quad (1.8)$$

$$\eta = \eta_{p,0} \left(1 + 2.0703 \times Hct + 3.7222 \times Hct^2 \right) \times \exp\left(-7.0276 \left(1 - \frac{Te_r}{Te} \right)\right) \quad (1.9)$$

The reference temperature is 296.16K with corresponding plasma viscosity 1.67×10^{-3} Pa s. This model is produced out of many data sets and has been successfully validated with other data sets.

Another example of a generalized Newtonian model is the Carreau model:

$$\sigma_{12} = \left[\eta_{\infty} + (\eta_0 - \eta_{\infty}) \left(1 + (t_c |\dot{\gamma}|)^2 \right)^{\frac{c-1}{2}} \right] \dot{\gamma} \quad (1.10)$$

At low shear rates the viscosity is η_0 , when $0 < c < 1$, the fluid is shear thinning, meaning that the viscosity decreases with increasing shear rate. When $c > 1$ the viscosity is shear thickening, meaning that the viscosity increases with increasing shear rate. At high shear rates the viscosity converges asymptotically to η_{∞} . Figure 1.7 shows the behavior of the Carreau model conceptually for a shear thinning fluid.

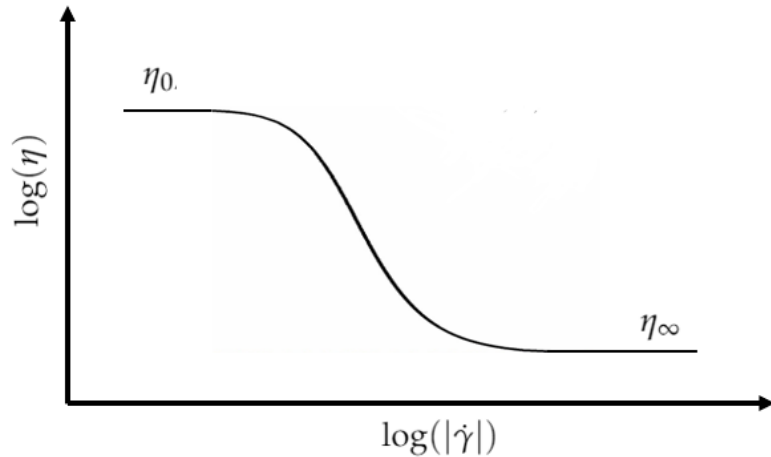


Figure 1.7: Logarithmic plot of the viscosity versus the shear rate for a shear thinning fluid according to the Carreau model.

The parameters for the generalized Newtonian models are mostly used as fitting parameters for experimental data but are not connected to a deeper physical meaning.

1.3.2 Viscoelastic Models

General Newtonian fluids are entirely viscous, meaning that all the kinetic energy of the fluid is directly dissipated as heat when the fluid flows. Some fluids have both viscous and elastic properties. Meaning that the kinetic energy can first be stored into reversible elastic energy before being released in a reversible manner and dissipated as heat. When a fluid is almost purely elastic, it approaches the nature of an elastic solid. An elastic solid stores all its kinetic energy reversibly as elastic energy. When the force on the elastic solid is released, its form returns to its initial form. A purely elastic solid can be described by Hooke's law [2]:

$$\sigma_{12} = G\gamma \quad (1.11)$$

The simplest continuous model that captures viscoelastic behavior is the Maxwell model, which assumes that the fluid behaves as an elastic solid and a purely viscous liquid in series. This is also often imagined as a spring and a dashpot in series. So part of the input energy is temporarily stored as elastic energy and part of the input energy is dissipated into heat. The expression for the shear stress is obtained by combining equation 1.3 with constant viscosity and equation 1.11. The viscosity divided by the elastic modulus can be seen as a characteristic relaxation time t_m of the fluid. The linearized Maxwell model is given in equation 1.12.

$$t_m \frac{d\sigma}{dt} + \sigma = 2\eta \underline{D} \quad (1.12)$$

$$t_m = \frac{\eta}{G}$$

Again when the fluid is only sheared in one direction, this tensorial equation can be reduced to one scalar equation:

$$t_m \frac{d\sigma_{12}}{dt} + \sigma_{12} = \eta \dot{\gamma} \quad (1.13)$$

Because the coordinate system is fixed with the geometry and the fluid elements can stretch, in case the fluid has a normal stress difference, and rotate with the flow, it is more correct to use an upper-convected time derivative or Oldroyd derivative [31, 32]. This leads to the upper-convected Maxwell model (equation 1.14).

$$t_m \hat{\underline{\underline{\sigma}}} + \underline{\underline{\sigma}} = t_m \left(\frac{\partial \underline{\underline{\sigma}}}{\partial t} + \underline{\underline{v}} \cdot \underline{\underline{\nabla}} \underline{\underline{\sigma}} - (\underline{\underline{\nabla}} \underline{\underline{v}})^T \cdot \underline{\underline{\sigma}} - \underline{\underline{\sigma}} \cdot \underline{\underline{\nabla}} \underline{\underline{v}} \right) + \underline{\underline{\sigma}} = 2\eta \hat{\underline{\underline{D}}} \quad (1.14)$$

In this case the different scalar equations that make up the tensorial equation can no longer be decoupled as in the case of the Maxwell fluid. When the flow is in steady state and under shear, the upper-convected derivative applied to the shear component reduces to the regular (equation 1.13) derivative. In general the viscosity and the elastic modulus, and thus the time constant t_m can be a function of the stress tensor [32]:

$$t_m(\underline{\underline{\sigma}}) \hat{\underline{\underline{\sigma}}} + \underline{\underline{\sigma}} = 2\eta(\underline{\underline{\sigma}}) \hat{\underline{\underline{D}}} \quad (1.15)$$

1.3.3 Thixotropic Models

A thixotropic fluid has a continual decrease in viscosity with time when it is subjected to shear flow. The explanation for this can be traced back to a delaying microstructure [30]. When applied to blood, the longer the fluid is sheared, the more the rouleaux structure breaks down into individual RBCs, which lowers the viscosity. When the shear on the fluid is released, the original microstructure recovers. This is often modelled by introducing a parameter which is subject to a relaxation equation [30]. Because of the connection with the microstructure of the fluid, this parameter is often chosen to be a structural parameter going from 0, representing no structure, to 1, representing the maximally structured state of the fluid.

Initially two different paths have been followed by researchers [13, 30, 33]. The first path is a thixotropic extension of the yield stress approach, dividing the stress in an elastic and a viscous part.

$$\gamma = \gamma_e + \gamma_p \quad \Leftrightarrow \quad \dot{\gamma} = \dot{\gamma}_e + \dot{\gamma}_p \quad (1.16)$$

Both parts are governed by the microstructure and thus by a structural parameter which undergoes a relaxation equation. The structure of the fluid increases by Brownian motion, which is the dominant process when the flow is completely unstructured. Shearing the fluid can either lead to birth or death of RBC agglomerates depending on the shear rate. Typically aggregation is the main process at low shear rates, while breakdown becomes more dominant at high shear rates. An example of this approach is the AAB model developed by Apostolidis et al. [30]. The kinetic relaxation equation contains a Brownian aggregation term and a shear induced breakdown term:

$$\frac{d}{dt}\lambda = \frac{\sigma_\gamma}{\eta}k_\lambda \left((1 - \lambda) - \lambda \sqrt{\frac{4\eta\dot{\gamma}_p}{\sigma_0}} \right) \quad (1.17)$$

For this model the structure of the fluid influences only the elastic part through a kinetic equation for the elastic modulus G , which varies between G_0 at $\lambda = 1$ and 0 at $\lambda = 0$:

$$\begin{aligned} \sigma_{12} &= G\gamma_e + \eta\dot{\gamma}_p & (1.18) \\ \frac{d}{dt}G &= \frac{\sigma_\gamma}{\eta}k_G\lambda(G_e - G) \\ \sigma_\gamma &\equiv G_0\gamma_{e,0} \\ G_e &= \lambda G_0 \end{aligned}$$

In this model, the material becomes purely viscous when no more structure is left ($\lambda = 0$). When the fluid is at its maximal structure, the elastic stress is equal to the yield stress. The elastic strain varies from $\gamma_{e,0}$ when the fluid is fully structured to $\gamma_{e,max}$ when it has stored its maximal amount of elastic energy. For fluids which have a very high value for $\gamma_{e,\infty}$, the maximum elastic strain is taken as $\gamma_{e,0}/\lambda^2$.

$$\begin{aligned} \dot{\gamma}_e &= \dot{\gamma}_p - \frac{\gamma_e}{\gamma_{e,max}}|\dot{\gamma}_p| & (1.19) \\ \gamma_{e,max} &= \min \left(\frac{\gamma_{e,0}}{\lambda^2}, \gamma_{e,\infty} \right) \end{aligned}$$

In steady state, equation 1.18 converges to the Casson model (equation 1.6). Which is why the shear induced breakdown term is chosen to have that particular form in

equation 1.17.

The HAWB model, more recently developed by Horner et al. [13] has a modified shear induced breakdown term, because the authors did not attempt to converge to the Casson model in steady state as it is not completely accurate for blood flow, but only forms a good approximation. Moreover a shear induced agglomeration term is added:

$$\frac{d}{dt}\lambda = \frac{1}{t_\lambda} \left((1 - \lambda) + (1 - \lambda)t_a|\dot{\gamma}_p| - \lambda(t_b|\dot{\gamma}_p|)^2 \right) \quad (1.20)$$

The model consists of a thixotropic part and a viscoelastic part:

$$\underline{\underline{\sigma}} = \sigma_R + \underline{\underline{\sigma}}_C \quad (1.21)$$

It is written in tensorial form for the viscoelastic part, but the thixotropic part is not yet adapted to tensorial form. In the thixotropic part the structure influences both the elastic and the viscous part:

$$\sigma_R = \lambda G_R \gamma_e + \lambda^3 \eta_R \dot{\gamma}_p \quad (1.22)$$

The λ^3 proportionality to the thixotropic viscosity is chosen to better represent the link of the structure parameter to the average length of the rouleaux [13]. The elastic modulus of the thixotropic part G_R is also governed by a kinetic equation:

$$\frac{d}{dt}G_R = \frac{1}{t_G} \left(\frac{G_{0,R}}{\lambda} - G_R \right) \quad (1.23)$$

$$G_{0,R} = \frac{\sigma_\gamma}{\gamma_{0,R}}$$

The elastic strain builds up when the shear rate is increased until it reaches its maximum. The maximum elastic strain decreases however when the structure decreases.

$$\gamma_{e,max} = \gamma_{0,R} \lambda \quad (1.24)$$

$$\dot{\gamma}_e = \begin{cases} \dot{\gamma}_p - \frac{\gamma_e}{\gamma_{e,max}} |\dot{\gamma}_p| & \frac{d}{dt} \gamma_{e,max} \geq 0 \\ \dot{\gamma}_p - \frac{\gamma_e}{\gamma_{e,max}} |\dot{\gamma}_p| + \frac{\gamma_e}{\gamma_{e,max}} \frac{d}{dt} \gamma_{e,max} & \frac{d}{dt} \gamma_{e,max} < 0 \end{cases}$$

The viscoelastic part is an extended White-Metzner model, which is similar to the general form of the upper-convected Maxwell model (equation 1.15) with the specification that the dependence on the shear rate tensor is only represented in the form of the first Invariant. The first invariant of second-order tensor is equal to its trace.

$$\frac{\eta_C(I_{\sigma_C})}{G_C} \underline{\hat{\sigma}} + \underline{\sigma} = 2\eta_C(I_{\sigma_C}) \underline{\hat{D}} \quad (1.25)$$

G_C can be seen as the elastic modulus of one red blood cell. Because the original White-Metzner approach can have an incapability to extract structural information from the model, the extended white-Metzner model is used. For one dimensional shear flow, the stress tensor is assumed to be of the form:

$$\underline{\underline{\sigma}}_C = \begin{pmatrix} \sigma_{11,C} & \sigma_{12,C} & 0 \\ \sigma_{12,C} & 0 & 0 \\ 0 & 0 & 0 \end{pmatrix} \quad (1.26)$$

Thus the first invariant is equal to $\sigma_{11,C}$. The dependence of the viscosity on the first invariant of the stress tensor is expressed as follows:

$$\eta_C(I_{\sigma_C}) = \frac{-b - \sqrt{b^2 - 4c}}{2} \quad (1.27)$$

$$b = t_C \sqrt{\frac{G_C \sigma_{11,C}}{2}} - \eta_{0,C}$$

$$c = \eta_{\infty} t_C \sqrt{\frac{G_C \sigma_{11,C}}{2}}$$

To make the model converge to a cross model for steady state $\sigma_{11,ss,C} = \frac{2\eta_{ss,C}^2 \dot{\gamma}^2}{G_C}$. For shear flow in one direction equation 1.25 can be written as:

$$\sigma_{12,C} + \frac{\eta_C(I_{\sigma_C})}{G_C} \frac{d\sigma_{12,C}}{dt} = \eta_C(I_{\sigma_C}) \dot{\gamma} \quad (1.28)$$

and in steady state it converges to the cross model:

$$\sigma_{ss,12,C} = \eta_{ss,C}(|\dot{\gamma}|) \dot{\gamma} = \left(\frac{\eta_{0,C} - \eta_{\infty,C}}{1 + t_C |\dot{\gamma}|} + \eta_{\infty,C} \right) \dot{\gamma} \quad (1.29)$$

This model contains 11 model parameters: $\eta_{c,0}, \eta_{c,\infty}, \sigma_\gamma, t_a, t_b, t_c, t_\lambda, t_G, \mu_R, \gamma_{0,R}, G_C$, which are fitted using a multiparameter global optimization method based on a parallel tempering algorithm. This model is able to fit steady shear stress data perfectly and has a close fit to UD-LAOS flow in most cases (see section 1.3.4).

The thixotropic models discussed so far are discontinuous because they have a variable yield stress below which the fluid does not move. The second common approach followed by researchers is to start from an upper-convected Maxwell model or White-Metzner model, which are pure viscoelastic models and include a function that is subject to a relaxation equation [34]. To model pulsating Poiseuille flow, a continuous shear stress model is needed, because the transient momentum equation is not compatible with a yield stress. When not subjected to any shear, the shear stress must be zero by definition. A yield stress is only a fitting parameter which matches the experimental data for experiments where the relaxation time of the system is much small than the observation time, as mentioned above. The thixotropic extension of the upper-convected Maxwell model (equation 1.14) is:

$$t_m \underline{\underline{\hat{\sigma}}} + \lambda \underline{\underline{\sigma}} = 2\eta \underline{\underline{D}} \quad (1.30)$$

This is equal to the upper-convected Maxwell model when $\lambda = 1$. An example of a thixotropic expansion is the MBM (modified Bautista-Manero) model [35]:

$$\lambda = 1 + k_1 k_2 \underline{\underline{\sigma}} : \underline{\underline{D}} \quad (1.31)$$

$$\frac{d}{dt} \lambda = \frac{1}{k_1} (1 - \lambda) + k_2 \underline{\underline{\sigma}} : \underline{\underline{D}}$$

The term corresponding to k_1 in the construction term in the relaxation equation and the term corresponding to k_2 the destruction equation. Another more recent approach by Stephanou et al. [33] is based on non-equilibrium thermodynamics. The model divides the shear term into a viscoelastic term, a structural term and an Oldroyd-B term respectively:

$$\underline{\underline{\sigma}} = G(\underline{\underline{\tilde{c}}} - \underline{\underline{\delta}}) - \frac{G}{2} \lambda \ln(\lambda) \underline{\underline{\tilde{c}}} + 2\eta_s \underline{\underline{D}} \quad (1.32)$$

A dimensionless conformation tensor is introduced to gain more freedom in the formulation of the model. In this model, it satisfies the equation:

$$\hat{\underline{\underline{c}}} = -\frac{1-\lambda}{t_C}(\underline{\underline{c}} - \underline{\underline{\delta}}) \quad (1.33)$$

This gives the viscoelastic term a thixotropic and shear thinning character. The relaxation equation for the structural parameter is:

$$\frac{D\lambda}{Dt} = -\frac{1}{t_\lambda} \ln(\lambda) - (\underline{\underline{\nabla v}}^T : \underline{\underline{c}})\lambda \quad (1.34)$$

Overall this model has only 4 parameters: G, η_s, t_C and t_λ , but it is able to capture the viscoelastic, thixotropic and shear thinning nature of blood.

1.3.4 UD-LAOS Flow

UD-LAOS means unidirectional large amplitude oscillatory shear. Meaning that the shear has the form:

$$\gamma = \gamma_{SS}(1 + \epsilon \sin(\omega t)) \quad (1.35)$$

This is a form of pulsatile flow, which is the superposition of a steady state part and an oscillating part. The results for UD-LAOS flow are often presented in Bowditch-Lissajous plots. Often the 2-dimensional projections of the Lissajous plot are studied (Figure 1.8). They either plot the shear stress against the shear or plot the shear stress against the shear rate. The plot of the shear rate versus the shear is always a circle because the shear rate is the derivative of the shear and is therefore always 90 degrees out of phase compared to the shear. Figure 1.8 shows 2-dimensional projections of the shear stress versus the strain for different frequencies using the model developed by Horner et al. [13].

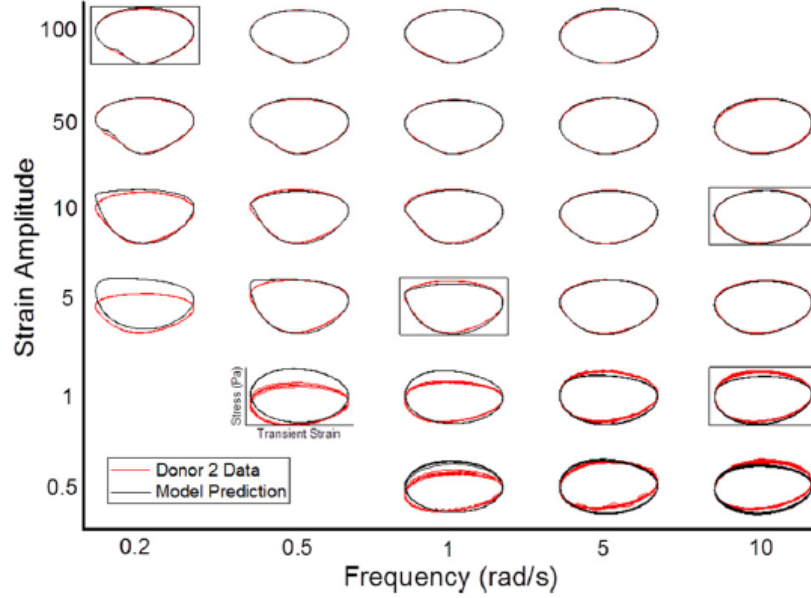


Figure 1.8: 2-dimensional projections of the shear stress versus the strain for different frequencies using the model developed by Horner et al. [13]²

In the human body the blood flow has a pulsating behavior, which can be approximated by pressure driven UD-LAOS flow instead of shear driven UD-LAOS flow .

$$\frac{\partial p}{\partial z} = \frac{\partial p_{SS}}{\partial z} (1 + \epsilon \sin(\omega t)) \quad (1.36)$$

Because the time dependence of the pressure drop per unit length is purely sinusoidal, the momentum equation (1.1) can be solved much more easily by taking the Fourier transform and making use of the following Fourier characteristic:

$$\mathcal{F}\left\{\frac{\partial v}{\partial t}\right\} = i\omega\mathcal{F}\{v\} \quad (1.37)$$

By doing this, it is possible to directly eliminate the time derivative. If two of the three spatial dimensions can be eliminated as well by choosing an appropriate geometry and conditions for the problem, equation 1.1 becomes an ordinary differential equation (ODE). If the ODE is linear, it is possible to find an analytical solution. This scenario is the case for flow in a tubular vessel, like a blood vessel, if

² Reprinted with permission from [13]. Copyright 2018, The Society of Rheology.

fully developed flow is assumed. This means that the blood vessel is assumed long enough that there is no more variation in the direction parallel to the central axis of the cylindrical vessel, i.e. no entrance effects are taken into account. The Maxwell model (equation 1.12) is linear and has the following analytical solution for the axial velocity [36]:

$$v(r, t) = \Re \left[\left(\frac{R^2}{4\eta} \left(1 - \left(\frac{r}{R} \right)^2 \right) + \frac{1 - i\omega t_m}{\eta\beta^2} \left(1 - \frac{J_0(\beta r)}{J_0(\beta R)} \right) \sin(\omega t) \right) \frac{dp}{dz} \right] \quad (1.38)$$

$$\beta = \sqrt{\frac{\rho((\omega t_m)^2 + i\omega t_m)}{\eta t_m}}$$

In the limit this solution contains both the Newtonian solution and the solution for an elastic solid. The Newtonian solution is obtained by setting the relaxation time to zero, because a purely viscous fluid has no relaxation time:

$$v(r, \omega) = \Re \left[\left(\frac{R^2}{4\eta} \left(1 - \left(\frac{r}{R} \right)^2 \right) - \frac{i}{\rho\omega} \left(1 - \frac{J_0(\beta r)}{J_0(\beta R)} \right) \sin(\omega t) \right) \frac{dp}{dz} \right] \quad (1.39)$$

$$\beta = \sqrt{\frac{\rho i \omega}{\eta}}$$

The other limiting case of a purely elastic fluid is found by taking the limit for t_m and η going to infinity and by using the relationship $t_m = \eta / G$.

$$v(r, \omega) = \Re \left[\left(\frac{-i}{\rho\omega} \left(1 - \frac{J_0(\beta r)}{J_0(\beta R)} \right) \right) \frac{dp}{dz} \sin(\omega t) \right] \quad (1.40)$$

$$\beta = \sqrt{\frac{\rho}{G}} \omega$$

The derivation of this expression is given in Appendix B. The expressions for the Newtonian fluid and that of the purely elastic fluid have a similar form for a pulsating pressure gradient, but a purely elastic fluid has no steady state velocity, because a solid remains its shape in steady state until the pressure drop is removed. These equations are of course only valid for laminar flow. A. F. Stalder et al. [37] found through MRI scans that flow instabilities in the aorta started to occur around critical Reynolds numbers of 4000. This is taken as reference critical Reynolds number throughout this thesis.

Chapter 2

PROBLEM DESCRIPTION AND METHODS

2.1 Problem Description

As said in the introduction, the momentum balance and the mass conservation balance can be greatly simplified by choosing an appropriate geometry and specific flow conditions. Figure 2.1 shows a schematic picture of the problem description. Nine assumptions are made:

1. blood can be represented as homogeneous
2. blood is incompressible
3. the blood flow is isothermal
4. no wall slip, thus the velocity is zero at the wall
- 5 the driving force is a pulsatile pressure gradient in the z - direction, i.e:

$$\frac{\partial p}{\partial z}(t) = \frac{\partial p_{SS}}{\partial z}(1 + \epsilon \sin(\omega t)) \quad (2.1)$$

6. no gravitational forces taken into account
7. No entrance effects (no z -dependence), thus pseudo steady state
8. the blood vessel has a perfect symmetry in the θ -direction
9. the flow is laminar

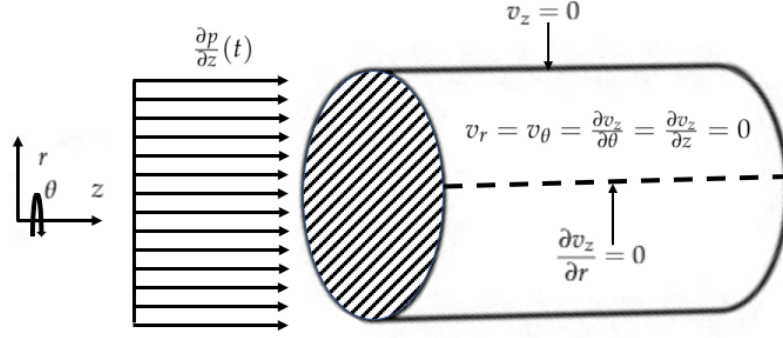


Figure 2.1: Schematic picture of the system geometry and flow conditions.

Because of assumption 2, the momentum balance and mass conservation balance, equations 1.1 and 1.2 respectively, simplify to equation 2.2 and 2.3

$$\rho \left(\frac{\partial(\underline{v})}{\partial t} + \underline{v} \cdot \underline{\nabla v} \right) = -\underline{\nabla} p + \underline{\nabla} \cdot \underline{\underline{\sigma}} - \underline{g} \quad (2.2)$$

$$\underline{\nabla} \cdot \underline{v} = 0 \quad (2.3)$$

Because of assumption 8, all the derivatives with respect to θ are zero and all the derivatives with respect to r at the centerline are zero. And because of assumption 7, all the derivatives with respect to z are zero. Then because of equation 2.3 combined with assumption 4, v_r and all its derivatives are 0. Finally, because of assumption 5 the only equation of interest is the scalar equation in the z -direction and considering the other assumptions, equation 2.2 and 2.3 simplify to a single scalar partial differential equation:

$$\rho \frac{\partial v_z}{\partial t}(r, t) = -\frac{\partial p}{\partial z}(t) + \frac{\sigma_{rz}}{r}(r, t) + \frac{\partial \sigma_{rz}}{\partial r}(r, t) \quad (2.4)$$

This is solved with the boundary conditions $v_z(R, t) = 0$ and $\frac{\partial v_z}{\partial t}(0, t) = \dot{\gamma}(0, t) = 0$ and the periodic condition $v_z(r, 0) = v_z(r, T)$.

2.2 Methods

2.2.1 Output Variable Formulation

The proposed solution to equation 2.4 uses the method of separation of variables. The solution for each output variable y can be presented in the following way:

$$y(r, t) = \underline{A}(t)\mathbf{Y}\underline{B}(r) = \sum_{i=1}^{2n+1} \sum_{j=1}^m a_i(t)y_{i,j}b_j(r) \quad (2.5)$$

The time-dependent part is represented by a Fourier series of $2n + 1$ terms. The Fourier series approximation is chosen because the time dependence of the input is purely sinusoidal, meaning that the output will consist of a sinusoidal function with 1 harmonic if the model is linear and with multiple harmonics for non-linear systems. The radial part is represented by m Chebyshev polynomials T_m of the first kind. The Chebyshev polynomials are chosen because they are numerically well conditioned and because they minimize the error over a fixed interval [38].

$$\begin{aligned} y(r, t) = & y_{0,0}T_0 + y_{0,1}T_1 + y_{0,2}T_2 + \dots + y_{0,m}T_m \\ & + (y_{1,0}T_0 + y_{1,1}T_1 + y_{1,2}T_2 + \dots + y_{1,m}T_m) \sin(\omega t) \\ & + (y_{2,0}T_0 + y_{2,1}T_1 + y_{2,2}T_2 + \dots + y_{2,m}T_m) \cos(\omega t) \\ & + (y_{3,0}T_0 + y_{3,1}T_1 + y_{3,2}T_2 + \dots + y_{3,m}T_m) \sin(2\omega t) \\ & + (y_{4,0}T_0 + y_{4,1}T_1 + y_{4,2}T_2 + \dots + y_{4,m}T_m) \cos(2\omega t) \\ & + \dots \\ & + (y_{2n-1,0}T_0 + y_{2n-1,1}T_1 + y_{2n-1,2}T_2 + \dots + y_{2n-1,m}T_m) \sin(n\omega t) \\ & + (y_{2n,0}T_0 + y_{2n,1}T_1 + y_{2n,2}T_2 + \dots + y_{2n,m}T_m) \cos(n\omega t) \end{aligned} \quad (2.6)$$

Another advantage of the Chebyshev polynomials is the computational efficiency for generating higher order Chebyshev polynomials through the recursive relationship:

$$T_{m+1}(r) = 2rT_m(r) - T_{m-1}, \quad T_0 = 1, \quad T_1(r) = r \quad (2.7)$$

The derivatives of the Chebyshev polynomials can also be found by deriving this recursive equation. The coefficients $y_{i,j}$ are stored in \mathbf{Y} , which is a $2n + 1 \times m$ matrix.

For discrete solutions \mathbf{A} has $2n+1$ columns and as many rows as the number of discrete time points chosen. \mathbf{B} has m rows and as many columns as the number of radial points chosen.

$$\mathbf{A}(\underline{t}) = \begin{bmatrix} 1 & \sin \omega \underline{t} & \cos \omega \underline{t} & \sin 2\omega \underline{t} & \cos 2\omega \underline{t} & \dots & \sin n\omega \underline{t} & \cos n\omega \underline{t} \end{bmatrix} \quad (2.8)$$

$$\mathbf{Y} = \begin{bmatrix} y_{00} & y_{01} & y_{02} & \dots & y_{0m} \\ y_{10} & y_{11} & y_{12} & \dots & y_{1m} \\ \vdots & \vdots & \vdots & \ddots & \vdots \\ y_{n0} & y_{n1} & y_{n2} & \dots & y_{nm} \end{bmatrix}$$

$$\mathbf{B}(\underline{r}) = \begin{bmatrix} T_0 & T_1(\underline{r}) & T_2(\underline{r}) & \dots & T_m(\underline{r}) \end{bmatrix}^T$$

This representation is best for every output parameter where no additional condition is known about, such as the structural parameter. For the displacement z and its derivatives like the axial velocity, the shear and shear rate, it is known that the a component of the displacement needs to be proportional to time and that there can be no displacement at $t = 0$. This means that an adapted Fourier series is necessary to fit the general solution for pulsatile flow. Because of the symmetry of the problem the oscillating input always has an oscillating output, which means that the constant Fourier term is always zero for the oscillating part. For the time-constant component the velocity is constant in time thus the displacement z of this component is linear in time. As a consequence, the first term in the Fourier series needs to be proportional to t . This leads to an adapted matrix \mathbf{A} for the output variable z :

$$\mathbf{A}_z(\underline{t}) = \begin{bmatrix} \underline{t} & \sin \omega \underline{t} & \cos \omega \underline{t} & \sin 2\omega \underline{t} & \cos 2\omega \underline{t} & \dots & \sin n\omega \underline{t} & \cos n\omega \underline{t} \end{bmatrix} \quad (2.9)$$

The velocity needs to be zero at the boundary and that the shear rate needs to be 0 at the centerline. A smart choice for the radial component \mathbf{B}_z of z to make the computation more efficient and include the boundary conditions at once is thus to multiply every term by $1 - r^2$. Because of the cylindrical symmetry of the problem, only the even Chebyshev polynomials are enough to represent the radial part.

$$\mathbf{B}_z = \begin{bmatrix} T_0(1 - \underline{r}^2) & T_2(1 - \underline{r}^2) & T_4(1 - \underline{r}^2) & \dots & T_{2m}(1 - \underline{r}^2) \end{bmatrix}^T \quad (2.10)$$

The shear stress always needs to be zero at the centerline. So the radial polynomials for the shear rate can be made more efficient by multiplying every polynomial with r . Also because of the cylindrical symmetry, only the uneven polynomials are necessary to represent the shear stress. This gives for \mathbf{B}_t of σ_{rz} :

$$\mathbf{B}_t = \left[T_{0r} \quad T_{2r} \quad T_{4r} \quad \dots \quad T_{2mr} \right]^T \quad (2.11)$$

2.2.2 Making the Problem Dimensionless

All the equations are converted to the dimensionless domain using the Buckingham Pi-theorem. With the right choice of parameters to make the problem dimensionless, the terms in the momentum balance (equation 2.4) are of the same order of magnitude, which makes the problem numerically better conditioned. The other advantage of the dimensionless approach is to have one solution that fits all geometries. These solutions are of course only valid as long as the dimensionless parameters stay within limits that are physically reasonable. By example if the Reynolds number becomes too large a transition to turbulence occurs and the laminar flow solution is no longer valid. For a linear model, the time-constant component corresponds to the steady state solution, but this is not guaranteed when the model is non-linear.

Table 2.1 shows how the parameters are made dimensionless. There are 3 basic units: time, length and weight. The parameters chosen to make the other parameters dimensionless are the angular velocity for the time scale, the tube radius for the length scale and the viscosity for the weight scale.

Table 2.1: Examples of dimensionless numbers in a tubular vessel for fully developed axially pulsating Poiseuille flow.

Meaning	With dimensions	Dimensionless
Radius	r	$\tilde{r} = r/R$
Time	t	$\tilde{t} = t\omega$
Axial velocity	v_z	$\tilde{v}_z = v_z/(\omega R)$
Pressure gradient	$\frac{dp}{dz}$	$\frac{d\tilde{p}}{d\tilde{z}} = \frac{dp}{dz}/(\eta\omega/R)$
Shear rate	$\dot{\gamma}$	$\tilde{\gamma} = \dot{\gamma}/\omega$
Shear stress	σ	$\tilde{\sigma} = \sigma/(\eta\omega)$

In this way the momentum balance (2.4) in dimensionless form is defined by a Womersley number and a dimensionless pressure gradient:

$$Wo^2 \frac{\partial \tilde{v}_z}{\partial \tilde{t}}(\tilde{r}, \tilde{t}) = -\frac{d\tilde{p}}{d\tilde{z}}(1 + \sin(\tilde{t})) + \frac{\tilde{\sigma}_{rz}}{\tilde{r}}(\tilde{r}, \tilde{t}) + \frac{\partial \tilde{\sigma}_{rz}}{\partial \tilde{r}}(\tilde{r}, \tilde{t}) \quad (2.12)$$

$$\tilde{v}_z(1, \tilde{t}) = 0 \quad \tilde{\gamma}(0, \tilde{t}) = 0 \quad \tilde{v}_z(\tilde{r}, 0) = \tilde{v}_z(\tilde{r}, 2\pi)$$

$$Wo = \sqrt{\frac{\rho\omega R^2}{\eta}}$$

The Womersley number represents the ratio of the transient inertial force and the viscous force. Its definition is thus very closely related to the Reynolds number. The Womersley number and the dimensionless pressure drop determine together the shear stress at the wall and the angular frequency, yo compare results of shear flows with results of Poiseuille flows. The Womersley number and the dimensionless pressure drop can a posteriori be converted to a Weissenberg number ($Wi = \dot{\gamma}_w t_m$) and Deborah number ($De = \omega t_m$), given that the kinematic viscosity, relaxation time of the fluid and the tube radius are known.

2.2.3 Solving the Equations

To solve for all the different output parameters $y_{i,j}$, a collocation approach is used. This means that the polynomials are forced to fit the exact solution at a set of points in time and space. To have as much equations as variables, equation 2.12 must be solved for $2n + 1$ time points and m radial points. Leading to a total of $(2n + 1)m$ equations per output variable. The time points are taken equidistant, but the radial points are chosen to be the Chebyshev points t_k :

$$t_k = \cos\left(\frac{(2k + 1)\pi}{2(m + 1)}\right), \quad k = 0, \dots, m \quad (2.13)$$

These points are the roots of T_{m+1} and lie on the open interval $] - 1, 1[$, but they can be transformed to any other interval using a linear coordinate transformation. They are distributed more closely to the boundaries of the interval. The use of Chebyshev points results in a better error distribution across the interpolation interval and leads to convergence for every function with a shape that is smooth enough [38]. When this is not the case, e.g. for very steep curves, a coordinate transformation can be applied to allocate more points in regions where the curve is very non-linear. Such a numerically difficult situation occurs when calculating the velocity profile at high shear rates. The highest shear rates occur towards the edge creating a very steep velocity profile. The following Quadratic bilinear coordinate transformation can allocate more points towards the edge and maintains the cylindrical symmetry of the system via its quadratic terms. The transformation is carried out in dimensionless coordinates, meaning that r' and r vary between zero and unity:

$$r'^2 = \frac{(\alpha + 1)r^2}{\alpha r^2 + 1} \quad (2.14)$$

$$\alpha = \frac{0.5 - r_b^2}{0.5r_b^2}$$

When r_b^2 is one half, there is no coordinate transformation, but the closer r_b^2 comes to zero, the more points are allocated towards the edge. Figure 2.2 shows this clearly for $r_b^2 = 0.1$.

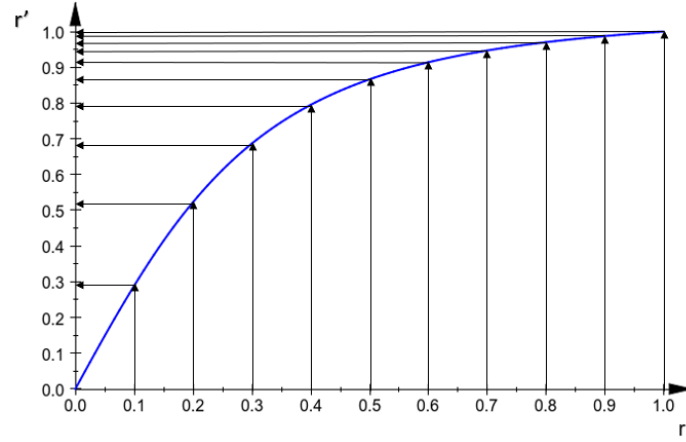


Figure 2.2: Quadratic bilinear coordinate transformation according to equation 2.14 with $r_b^2 = 0.1$.

Another advantage is that zero can never be a Chebyshev point, avoiding singularities in the calculations at the centerline of the tubular vessel. All the variables y are represented according to equation 2.6 and plugged into the equations. The equations are subsequently solved using Newton's method. Because this method does not always converge, zero order parameter continuation is used. This is most necessary for t_b in the lambda relaxation equation (3.15) and for λ itself, e.g. by introducing a continuation parameter cp in the conformation equation (1.33) with cp ranging from 0 (no thixotropic coupling) to 1 (full thixotropic coupling):

$$\hat{\underline{c}} = -\frac{1 - cp\lambda}{t_C}(\underline{\tilde{c}} - \underline{\delta}) \quad (2.15)$$

The Jacobian \mathbf{J} of the set of equations $\underline{F}(\underline{x})$ is approximated numerically by:

$$J_{i,j} = \frac{\partial F_i}{\partial x_j} = \frac{F_i(\underline{x} + \alpha \underline{\delta}_j) - F_i(\underline{x})}{\alpha} \quad (2.16)$$

$\underline{\delta}_j$ is a unit vector with 1 as its j -th element. α is taken 10^{-6} , which is small enough for the required accuracy for Newton's method, but not too small to avoid having a large finite difference error. The advantage of using polynomials is that the derivatives and integrals can be calculated exactly in an analytic way, making the method

semi-analytic. When deriving with respect to time only \mathbf{A} must be derived with respect to time and equivalently for radial derivatives, the derivative of \mathbf{B} with respect to r must be taken. For example the shear rate can be represented as follows:

$$\dot{\gamma}(r, t) = \frac{d\mathbf{A}(t)}{dt} \mathbf{Z} \frac{d\mathbf{B}(r)}{dr} = \sum_{i=1}^{2n+1} \sum_{j=1}^m \frac{a_i(t)}{dt} z_{i,j} \frac{b_j(r)}{dr} \quad (2.17)$$

The only error occurring in the model besides the machine error is the interpolation error. Finite difference methods have mainly the formulation error as well as the finite difference error which becomes increasingly large when the distance between the discrete points becomes smaller. Additionally there is also the error of the ODE-solver for transient problems, but this is eliminated in this model by use of the Fourier transform. That is why it is expected that the method proposed in this thesis will perform better than the finite difference error when the interpolation error is kept smaller than the formulation error. The computational code is included in Appendix D.

2.3 Figure Representation in the Results Section

Because of the cylindrical symmetry and the steady state assumption, the output variables for all θ - and z -values are the same. This means that the output variables are only function of the radius and time. A convenient way to represent the result is by imagining the front of the cylinder as a clock and drawing the radial axis as an arrow pointing from the center to 12 o' clock. thus the bottom of the plot represents the centerline and the top represents the edge. The magnitude of this output variable can then be represented on the axis orthogonal to this arrow. Output variables at different time points are plotted as separate curves. Figure 2.3 sketches this more clearly.

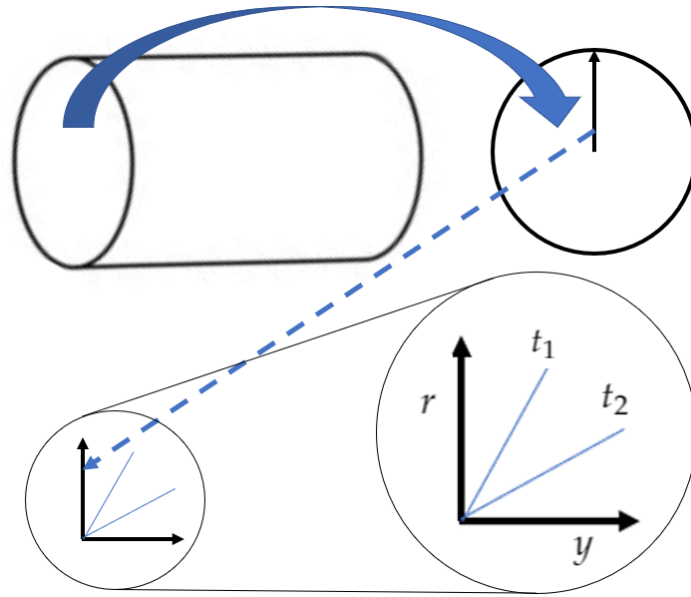


Figure 2.3: Schematic depiction of output variable representation.

Chapter 3

RESULTS AND DISCUSSION

3.1 Method Validation

This section shows the validation of the proposed computational model in section 2.2. First for a Newtonian fluid, then for a purely elastic fluid, followed by a Maxwell fluid and finally for a non-linear power law model.

3.1.1 Newtonian Fluid

The results in this section are calculated with the parameters in Table 3.1 for pulsating flow, i.e.:

$$\frac{dp}{dz} = \frac{dp_{SS}}{dz}(1 + \sin(\omega t)) \quad (3.1)$$

Table 3.1: Physical parameters used in result section for a Newtonian fluid.

Physical Parameter	Value
R	10^{-4} [m]
ρ	1200 [kg/m ³]
ω	9.42 [1/s]
$\frac{dp_{SS}}{dz}$	-2500 [Pa/m]
η	1.25×10^{-3} [Pa s]
$T = \frac{2\pi}{\omega}$	0.67 [s]

The Newtonian fluid is the most commonly used model in rheology because of its simplicity, but it does not capture the complex nature of blood. The solution for the Newtonian velocity profile, made dimensionless according to Table 2.1, can

be given in function of the Womersley number and the dimensionless pressure drop:

$$\bar{v}_z = \Re \left[\frac{1}{4}(1 - \bar{r}^2) - \frac{i}{Wo^2} \left(1 - \frac{J_0(Wo\sqrt{i}\bar{r})}{J_0(Wo\sqrt{i})} \right) \sin(\bar{t}) \right] \frac{d\bar{p}}{d\bar{z}} \quad (3.2)$$

$$Wo = \sqrt{\frac{\rho\omega R^2}{\eta}}$$

This velocity profile is shown in Figure 3.2 for $Wo = 0.3$ and $\frac{d\bar{p}}{d\bar{z}} = -21$. This gives a maximum Reynolds number of 8.5×10^{-4} , which is well below the critical value of 4000. These dimensionless values are based on the values in Table 3.1. The density of blood depends on the Hematocrit and the protein concentration [39]. An average estimation over different Hematocrit values and protein concentrations is made. The angular velocity is based on a heartbeat of 90/min. The tube radius is chosen to be small, because of the intention to be used in combination with experiments in the microfluidic device, but not too small to enter the regime where capillary forces dominate. The viscosity is taken as the solvent viscosity, i.e. the viscosity of plasma. The pressure drop per unit length is an approximate guess because it is hard to measure and differs depending on the place in the arterial network where it is measured. These parameters are thus estimates, but can be further refined when the modelling is combined with measurements from the microfluidic device. Figures 3.3 and 3.4 show the corresponding shear rate and shear stress respectively. Figure 3.1 shows how the axial velocity evolves in time. In this case the profile has only one harmonic because the Newtonian model is linear, but in general the time profile looks like a superposition of harmonics, but the time profile is always periodic. The profile also evolves differently in time for every radius. This applies also to all other output variables.

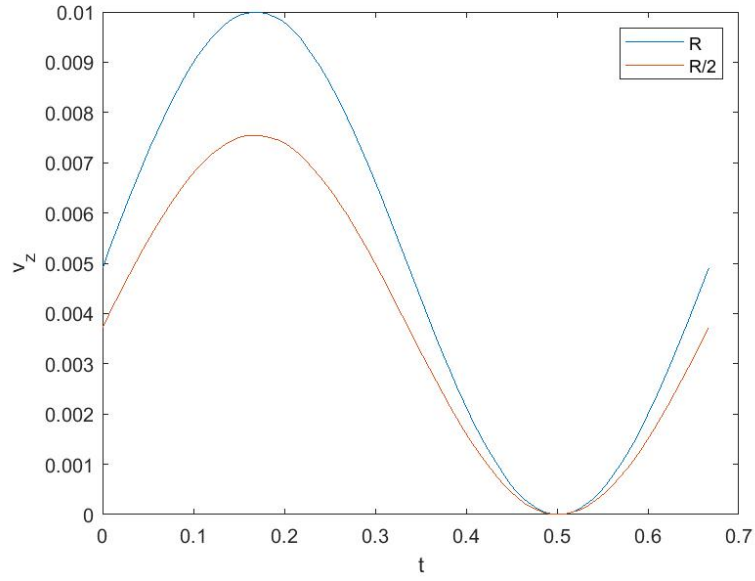


Figure 3.1: Newtonian axial velocity for pulsatile flow for $r = R$ (upper curve) and $r = R/2$ (lower curve) versus the time in SI-units.

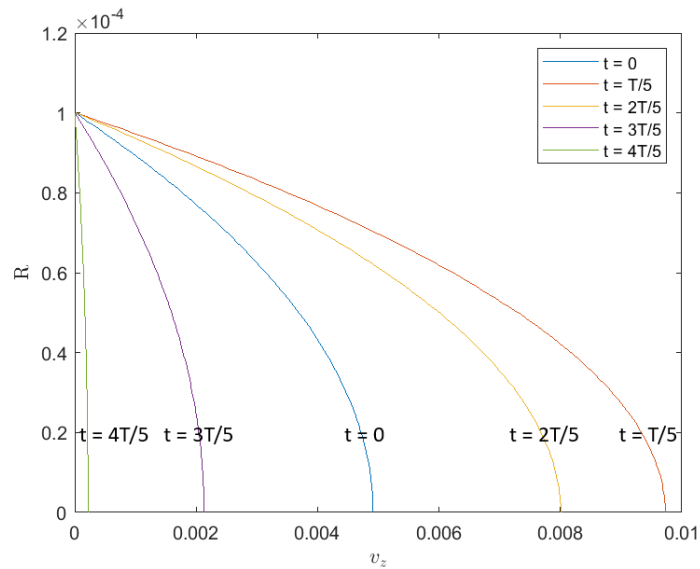


Figure 3.2: Newtonian axial velocity for pulsatile flow for 5 equidistant time points in the periodic domain in SI-units.

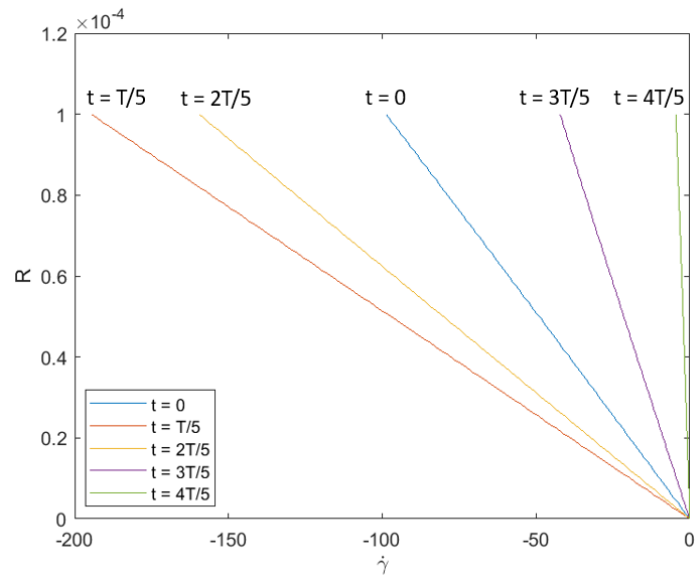


Figure 3.3: Newtonian shear rate for pulsatile flow for 5 equidistant time points in the periodic domain in SI-units.

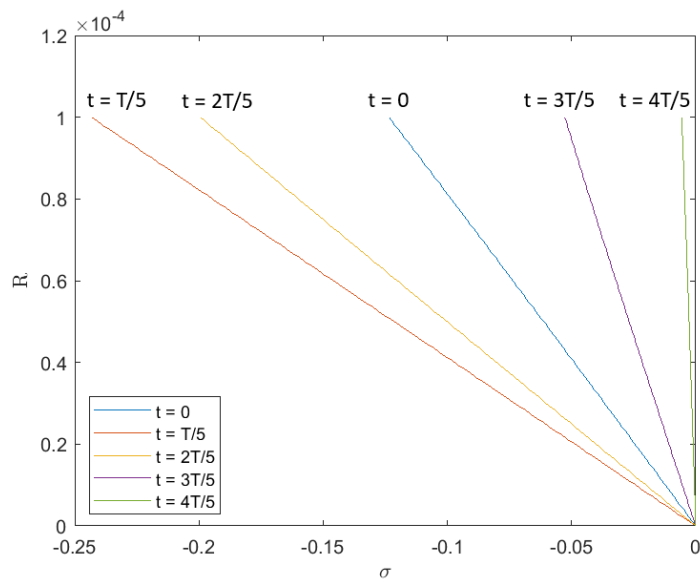


Figure 3.4: Newtonian shear stress for pulsatile flow for 5 equidistant time points in the periodic domain in SI-units.

The velocity profile at $t = 0$ is equal to the steady state profile. Figure 3.5 compares the absolute error for the collocation method with a second order finite

difference approach for the same number of unknowns that need to be solved for. the absolute error is defined as:

$$E = \frac{\sum_{r,t} |v_{z,numeric} - v_{z,analytic}|}{\text{total number of discrete points}} \quad (3.3)$$

The comparison between the collocation method and the finite difference method is also done with the same total number of discrete points, which need to be large enough to have a converging average absolute error. In this case it is taken to be 500.

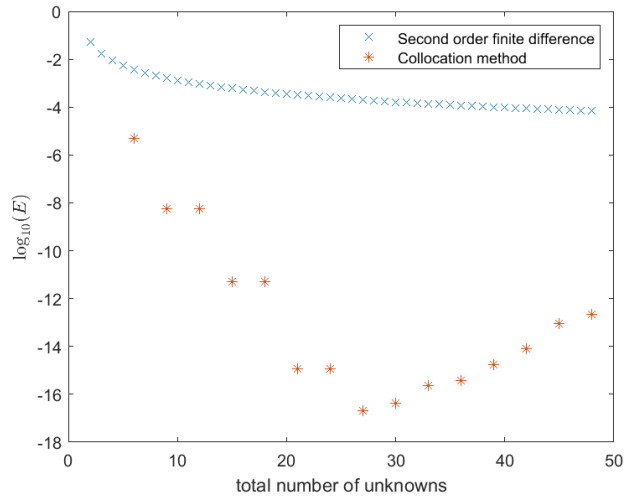


Figure 3.5: Error comparison for pulsatile flow between the collocation method and a second order finite difference method for the same number of equations that need to be solved.

The error of the collocation error is always smaller than the error of the second order finite difference method and it decreases much faster than with the total number of equations that need to be solved. When the order of the fitting polynomial becomes too high, the error starts to increase again. This is well known that the interpolation error increases for eventually when the order of polynomials becomes too high [38]. The collocation method can reach the machine error, while it is very hard for a finite difference method to reach below an error of 10^{-8} due to the finite difference error [38]. The computational cost for both methods is proportional to

the number of equations cubed, but the computational cost for the collocation algorithm is higher than for the finite difference approach when the same amount of equations need to be solved, due to more function evaluations per equation for the collocation method.

The 2D projection of the Lissajous plot in the shear stress-shear rate domain is a straight line as shown in Figure 3.6. Thus the shear stress and the shear rate are exactly in phase and this is another confirmation that the solution is correct.

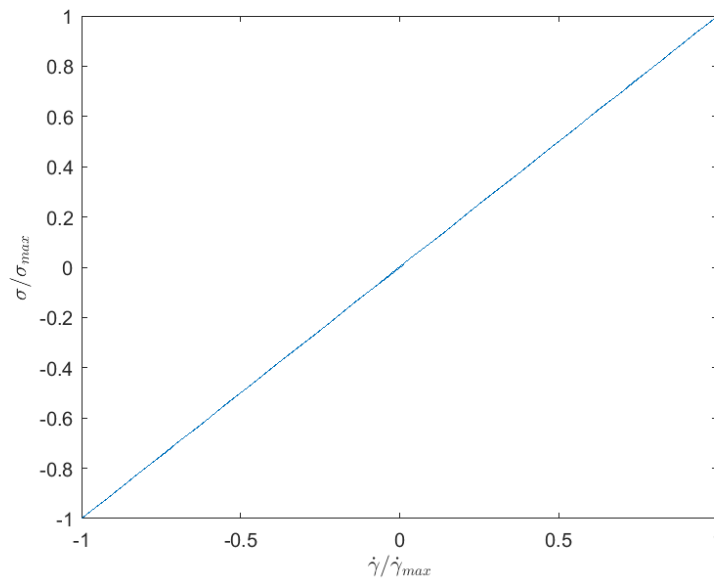


Figure 3.6: 2D projection of the Lissajous plot in the shear stress-shear rate domain for pulsatile flow for a Newtonian fluid.

3.1.2 Elastic Solid

The results in this section are calculated with the parameters in Table 3.2 for oscillatory flow, i.e.:

$$\frac{dp}{dz} = \frac{dp_{SS}}{dz} \sin(\omega t) \quad (3.4)$$

Table 3.2: Physical parameters used in result section for an elastic solid.

Physical Parameter	Value
R	10^{-4} [m]
ρ	1200 [kg/m ³]
ω	9.42 [1/s]
$\frac{dp_{SS}}{dz}$	-2500 [Pa/m]
G	10^{10} [Pa]
$T = \frac{2\pi}{\omega}$	0.67 [s]

The elastic solid is on the complete opposite range than the Newtonian fluid on the viscoelastic spectrum. In steady state an elastic solid does not move. For oscillatory motion the solution is thus the same as for pulsatile motion. Typically the amplitude of the oscillations is a lot lower for solids than for liquids, because they are a lot stiffer. The analytic solution in dimensionless form is:

$$\tilde{v}_z = \Re \left[-\frac{i}{Wo^2} \left(1 - \frac{J_0(Wo\tilde{r})}{J_0(Wo)} \right) \sin(\tilde{t}) \right] \frac{d\tilde{p}}{d\tilde{z}} \quad (3.5)$$

$$Wo = \sqrt{\frac{\rho\omega^2 R^2}{G}}$$

Notice the adapted definition of the Womersley number. Because G is typically a couple of orders of magnitude large than η , the velocity is typically a couple of orders of magnitude smaller. But the solution becomes more sensitive to the angular velocity, which appears now squared in the Womersley number. Because the oscillating part of equation 3.2 and equation 3.5 are similar except for the complex number in the Bessel function, the error function also looks very similar to Figure 3.5, but the condition of the problem is defined to great extent by the value of G . For very low values of G , the problem is numerically very ill conditioned and no solution can be found. For more realistic values for solids ($G = 10^8$ and higher, e.g., approximately 200 GPa for steel [40]), the problem is very well conditioned.

Even with solving for three unknowns, which is the minimum number of equations for the collocation method with $n = m = 1$, the value for the absolute error is already 4.2×10^{-15} , which is approximately the machine error. Figure 3.7 shows that the velocity is perfectly symmetric and oscillating. It is also indeed many orders of magnitude lower than in Figure 3.2. Figure 3.8 and 3.9 show the shear stress and the shear rate respectively. The 2D projection of the Lissajous plot in the shear stress-shear rate domain is however now a circle instead of a straight line, because the shear stress and the shear rate are exactly 90 degrees out of phase. This is shown in Figure 3.10.

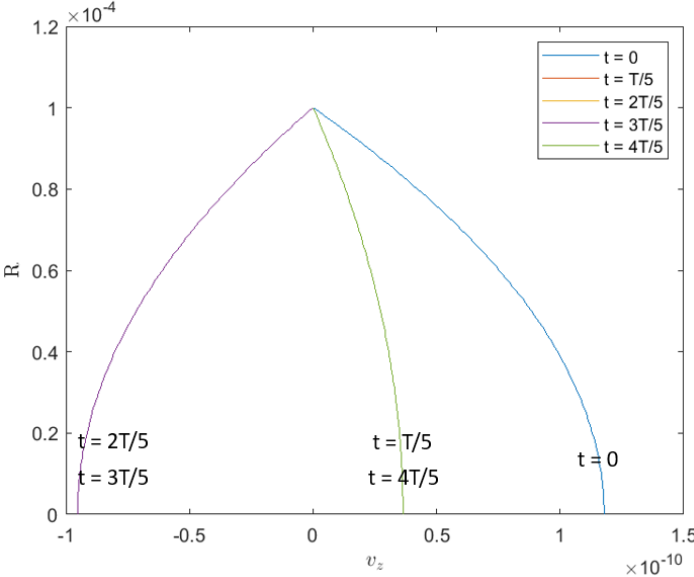


Figure 3.7: Axial velocity for oscillatory flow for an elastic solid for 5 equidistant time points in the periodic domain in SI-units.

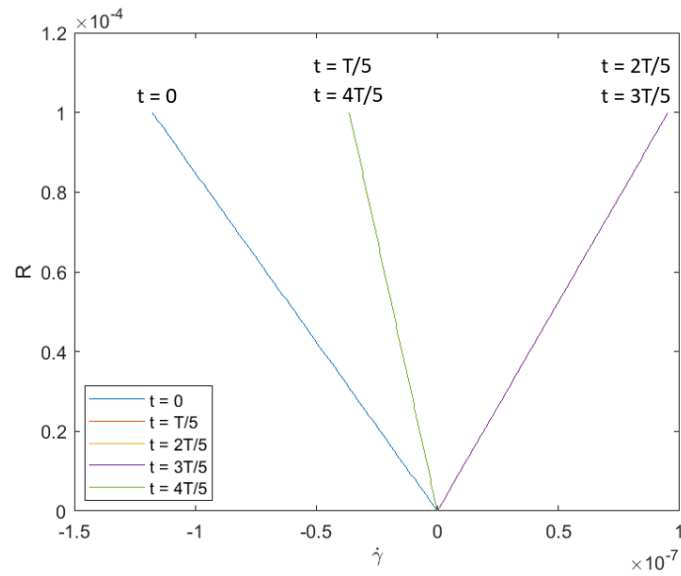


Figure 3.8: Shear rate for oscillatory flow for an elastic solid for 5 equidistant time points in the periodic domain in SI-units.

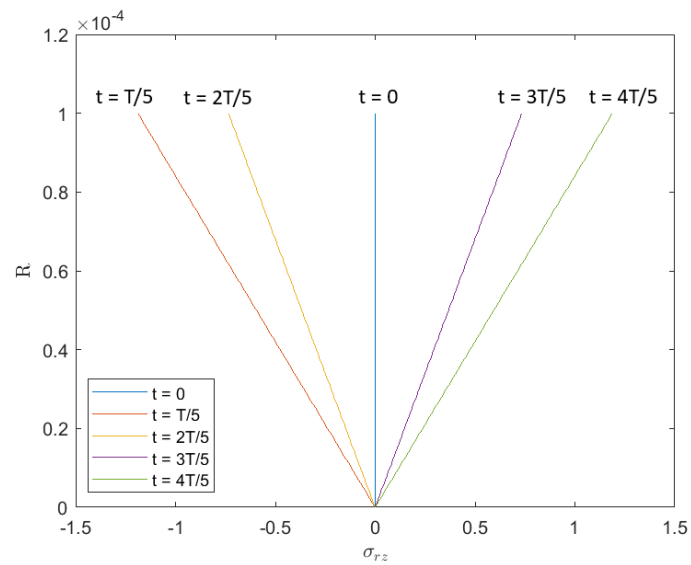


Figure 3.9: Shear stress for oscillatory flow for an elastic solid for 5 equidistant time points in the periodic domain in SI-units.

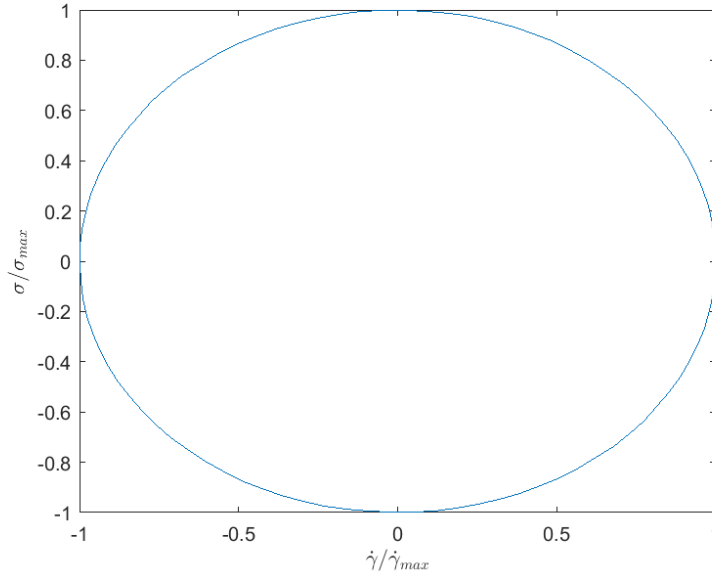


Figure 3.10: 2D projection of the Lissajous plot in the shear stress-shear rate domain for oscillatory flow for an elastic solid.

3.1.3 Maxwell Fluid

The results in this section are calculated with the parameters in Table 3.3 for pulsating flow, i.e.:

$$\frac{dp}{dz} = \frac{dp_{SS}}{dz} (1 + \sin(\omega t)) \quad (3.6)$$

Table 3.3: Physical parameters used in result section for a Maxwell fluid.

Physical Parameter	Value
R	10^{-4} [m]
ρ	1200 [kg/m ³]
ω	9.42 [1/s]
$\frac{dp_{SS}}{dz}$	-2500 [Pa/m]
η	1.25×10^{-3} [Pa s]
$T = \frac{2\pi}{\omega}$	0.67 [s]
t_m	0.1 [s]

The Maxwell fluid is a combination of the Newtonian fluid and the elastic solid and covers the entire viscoelastic spectrum in between them. The dimensionless analytical solution for the Maxwell equation is:

$$\tilde{v}_z = \Re \left[\frac{1}{4}(1 - \tilde{r}^2) - \frac{i}{Wo^2} \left(1 - \frac{J_0(Wo\sqrt{\tilde{t}_m + i\tilde{r}})}{J_0(Wo\sqrt{\tilde{t}_m + i})} \right) \sin(\tilde{t}) \right] \frac{d\tilde{p}}{d\tilde{z}} \quad (3.7)$$

Figure 3.11 shows the absolute error in function of the total number of unknowns for $Wo = 0.3$, $\frac{d\tilde{p}}{d\tilde{z}} = -21$ and $\tilde{t}_m = 0.2$

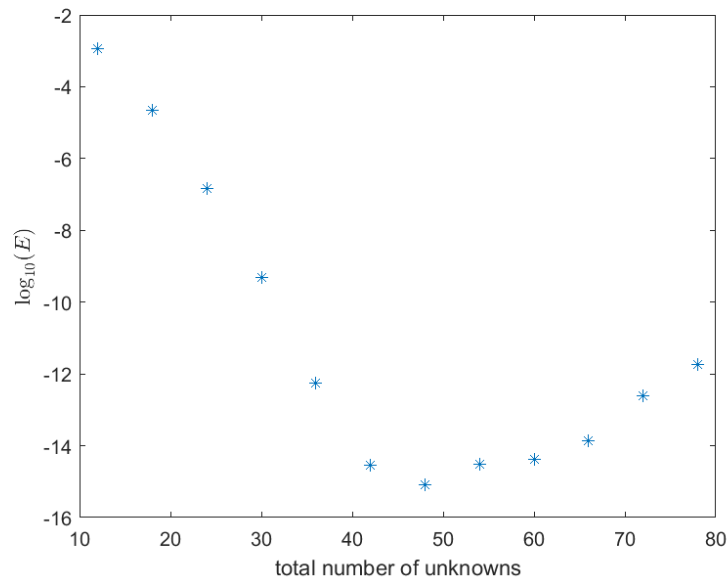


Figure 3.11: Absolute error for pulsatile flow for a Maxwell fluid with the collocation method, and $\tilde{t}_m = 0.2$.

For the Maxwell model, the shear stress can not anymore be written directly as function of the displacement, because of the derivative in the Maxwell model (equation 1.12). Thus there are two different outputs, the displacement and the shear stress. This means that the number of unknowns and equations doubles compared to solving for a Newtonian fluid, when using the same number of nodes. Figure 3.12 shows the velocity profile and Figures 3.13 and 3.14 show the shear rate and shear stress respectively.

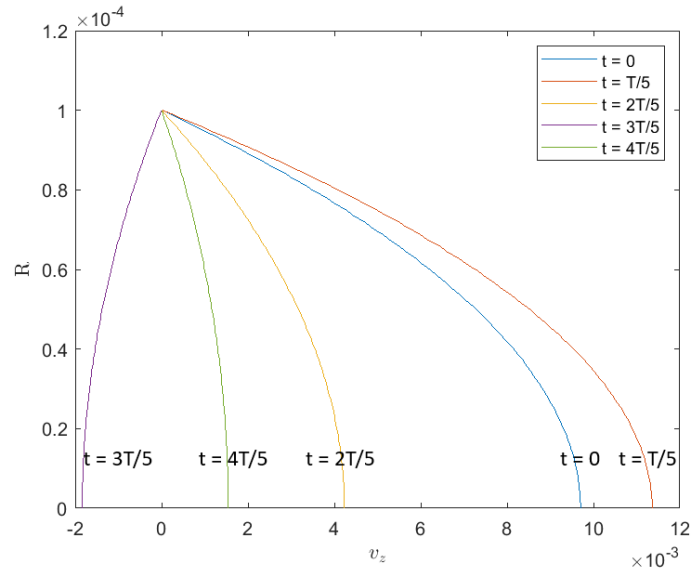


Figure 3.12: Axial velocity profile for a Maxwell fluid subjected to pulsatile flow for 5 equidistant time points in SI-units.

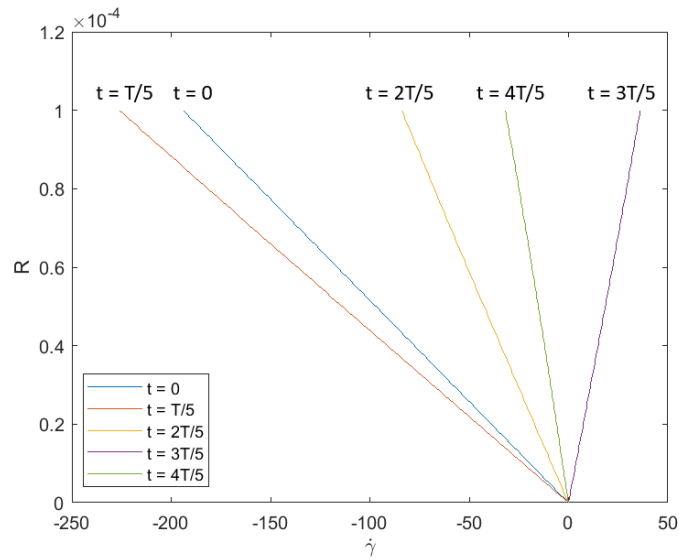


Figure 3.13: Dimensionless shear rate profile for a Maxwell fluid subjected to pulsatile flow for 5 equidistant time points in SI-units.

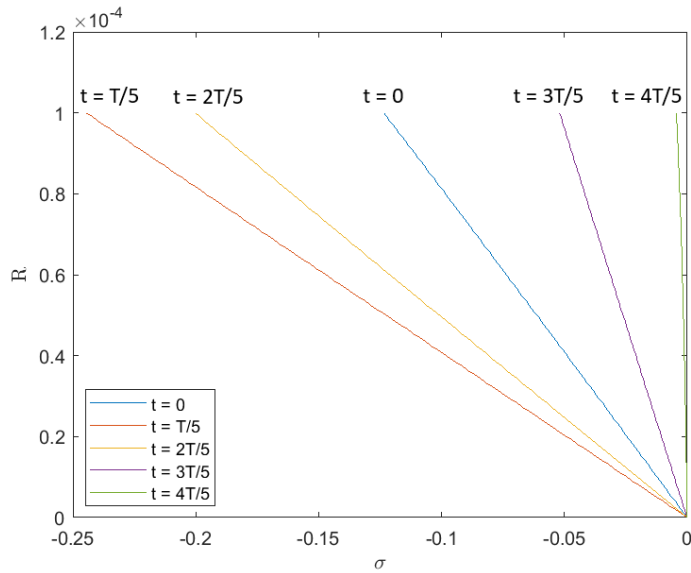


Figure 3.14: Dimensionless shear stress profile for a Maxwell fluid subjected to pulsatile flow for 5 equidistant time points in SI-units.

Viscoelasticity seems to increase the oscillating part of the axial velocity, giving rise to a higher maximum velocity and making even backflow possible. Figure 3.15 shows the 2D projection of the Lissajous plot in the shear stress-shear rate domain. The shape is now an ellipse, which is in between a circle and a straight line.

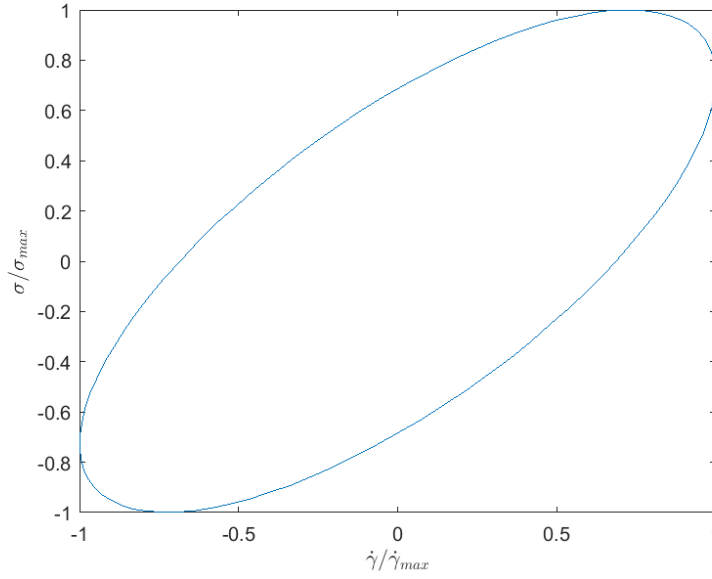


Figure 3.15: 2D projection of the Lissajous plot in the shear stress-shear rate domain for a Maxwell fluid subjected to pulsatile flow.

3.1.4 Power Law Model

The results in this section are calculated with the parameters in Table 3.4 for steady state flow, i.e.:

$$\frac{dp}{dz} = \frac{dp_{SS}}{dz} \quad (3.8)$$

Table 3.4: Physical parameters used in result section for a power law model.

Physical Parameter	Value
R	10^{-4} [m]
ρ	1200 [kg/m ³]
ω	9.42 [1/s]
$\frac{dp_{SS}}{dz}$	-2500 [Pa/m]
K	1.25×10^{-3} [Pa s ^q]
$T = \frac{2\pi}{\omega}$	0.67 [s]

The model is validated for the linear models. Only the steady state solutions can be compared for the non-linear power law model, because no transient analytical solution is available. The power law model has the following representation and is written down in scalar form:

$$\sigma = K(\dot{\gamma})^q \quad (3.9)$$

The units of K depend on the exponent q . The steady state solution for the power law model is [41]:

$$v_z = \left(-\frac{dp}{dz} \frac{R}{2K} \right)^{1/q} \frac{R}{1/q+1} \left[1 - \left(\frac{r}{R} \right)^{1/q+1} \right] \quad (3.10)$$

In dimensionless form, using Table 2.1, this becomes:

$$\tilde{v}_z = \left(-\frac{d\tilde{p}}{d\tilde{z}} \frac{1}{2\tilde{K}} \right)^{1/q} \frac{1}{1/q+1} \left[1 - r^{1/q+1} \right] \quad (3.11)$$

Figure 3.16 shows the dimensionless axial velocity profile for a power law fluid for $q = 0.2$. Because of the non-linearity and very steep velocity gradient, a coordinate transformation according to equation 2.14 is applied with $r_b = 0.1$.

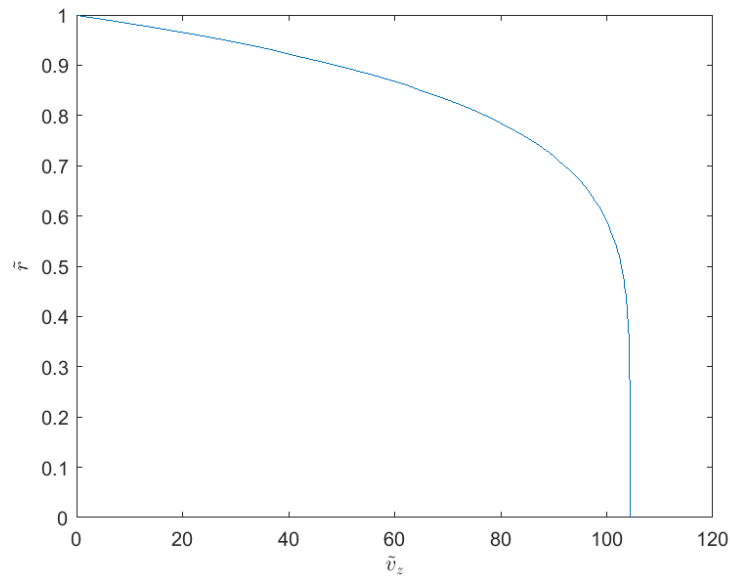


Figure 3.16: Dimensionless axial velocity profile for a power law fluid in steady state flow for $q = 0.2$.

For the steady state, the collocation model performs very well, with the error already going down to approximately the machine error after solving for 3 unknowns. When using polynomials of a too high order the interpolation error increases again. This is shown in Figure 3.17.

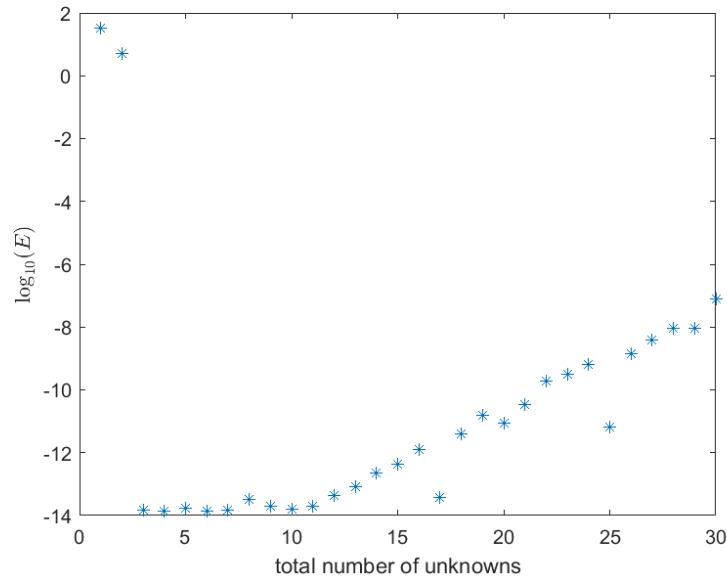


Figure 3.17: Absolute error of the collocation method in function of the number of unknowns for a power law fluid in steady state flow for $q = 0.01$.

Even for the extreme case of $q = 0.01$, a minimum absolute error of order 10^{-4} can be reached. The velocity profile for this case is shown in Figure 3.18 and it clearly shows a very steep velocity gradient. Also the fact that the velocity increases for a more shear thinning fluid becomes clear when comparing Figures 3.16 and 3.18. The absolute error in Figure 3.19.

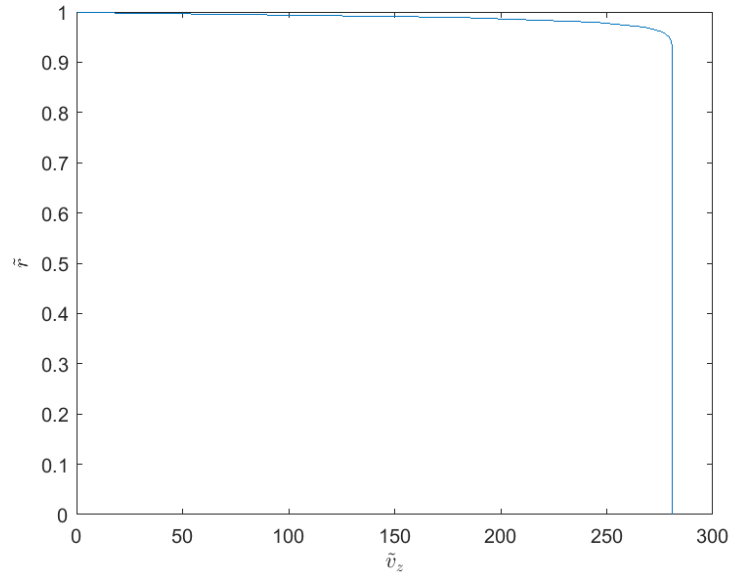


Figure 3.18: Dimensionless axial velocity profile for a power law fluid in steady state flow for $q = 0.01$.

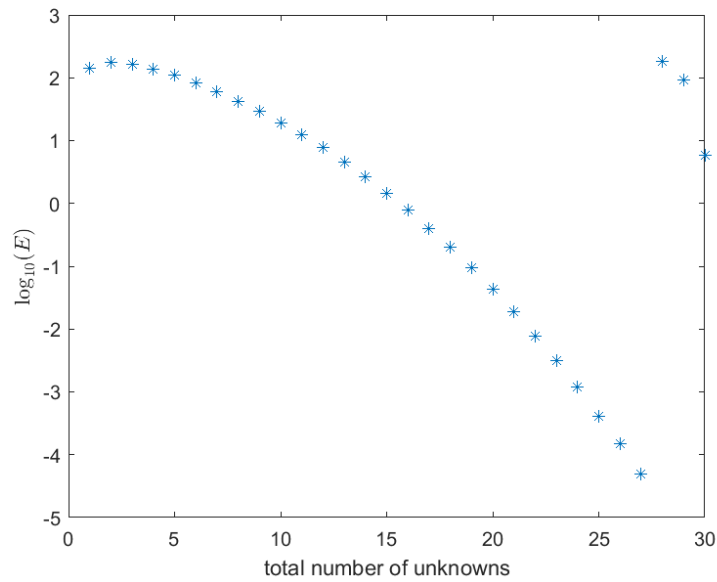


Figure 3.19: Absolute error of the collocation method in function of the number of unknowns for a power law fluid in steady state flow for $q = 0.01$.

3.1.5 Carreau Model

The results in this section are calculated with the parameters in Table ?? for oscillatory flow, i.e.:

$$\frac{dp}{dz} = \frac{dp_{SS}}{dz} \sin(\omega t) \quad (3.12)$$

Table 3.5: Physical parameters used in result section for a Carreau model.

Physical Parameter	Value
R	10^{-4} [m]
ρ	1200 [kg/m ³]
ω	9.42 [1/s]
$\frac{dp_{SS}}{dz}$	-2500 [Pa/m]
η_{∞}	1.2×10^{-3} [Pa s]
η_0	1 [Pa s]
$T = \frac{2\pi}{\omega}$	0.67 [s]
\tilde{t}_c	1 [-]

The previous section validates the model for the steady state power law case. When considering the transient case, the model becomes very poorly conditioned and a Carreau model (equation 1.10) is preferred over the power law model. The Carreau model converges to the power law model for large values of t_c with $K = \eta_0 t_c$, but is numerically better conditioned. The dimensionless scalar equation for the shear stress of the Carreau model is:

$$\tilde{\sigma} = 1 + \left(\frac{\eta_0}{\eta_{\infty}} - 1 \right) \left(1 + (\tilde{t}_c \tilde{\dot{\gamma}})^2 \right)^{\frac{q-1}{2}} \tilde{\dot{\gamma}} \quad (3.13)$$

The maximum exponent the collocation method can handle is $q = 0.1$ and this at a $Wi = De = 10$, but high such non-linearities usually do not occur. So the model is fine for handling non-linearities if the coordinate transformation is applied. Figure 3.20 and 3.21 show the dimensionless velocity and dimensionless shear rate profiles, for an oscillating velocity gradient in order to notice the strong non-linearity of

the shear rate profile. They were calculated using 10 harmonics and 16 Chebyshev nodes, meaning that the model needs to solve $(2n + 1)m = 336$ equations. Also 0^{th} order continuation needed to be used in combination with Newton's method to be able to find a solution. This high amount of equations makes the Jacobian very ill conditioned. The overall weak point of the collocation method is thus the ill-conditioned Jacobian. Any approach that improves the condition of the Jacobian can improve the algorithm. Nonetheless the conclusion is that the collocation method is a valid method for calculating complex blood flow under the conditions mentioned in section 2.1.

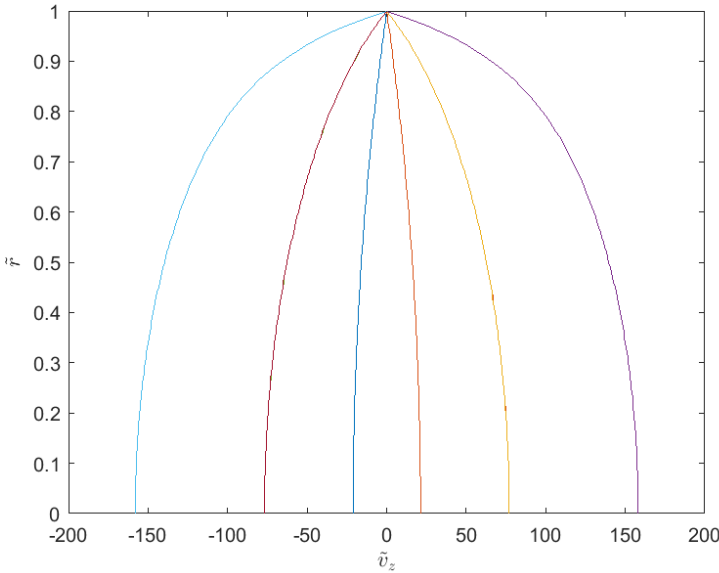


Figure 3.20: Transient dimensionless velocity profile for a Carreau fluid subjected with $q = 0.1$ and $Wi = De = 10$ for oscillating flow.

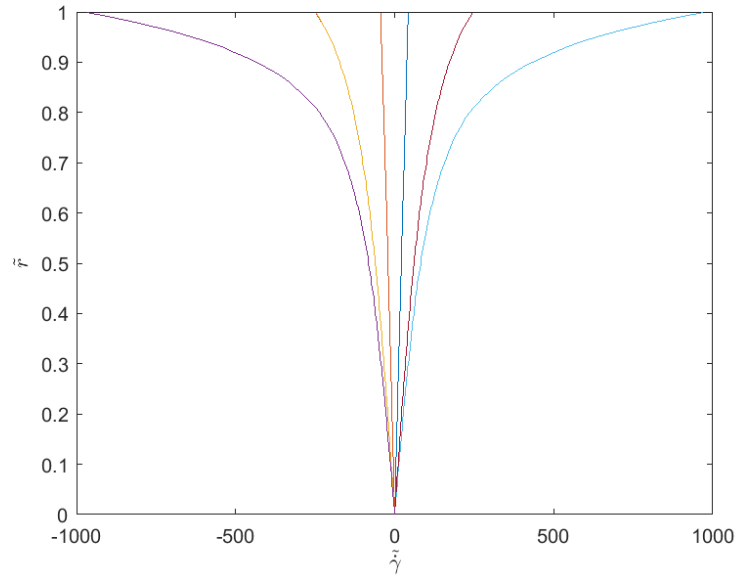


Figure 3.21: Transient shear rate profile for a Carreau fluid with $q = 0.1$ and $Wi = De = 10$ for oscillating flow.

3.2 Modified Stephanou model

The results in this section are calculated with the parameters in Table 3.6 for pulsatile flow, i.e.:

$$\frac{dp}{dz} = \frac{dp_{SS}}{dz} (1 + \sin(\omega t)) \quad (3.14)$$

Table 3.6: Physical parameters used in result section for the modified Stephanou model.

Physical Parameter	Value
R	10^{-4} [m]
ρ	1200 [kg/m ³]
ω	9.42 [1/s]
$\frac{dp_{SS}}{dz}$	-1500 [Pa/m]
G	1.9×10^{-2} [Pa]
$T = \frac{2\pi}{\omega}$	0.67 [s]
t_m	0.14 [s]
t_{lambda}	50 [s]
t_a	0 [s]
t_b	0.5 [s]

3.2.1 Structural parameter

To model thixotropy, next to shear thinning and viscoelasticity, using a parameter which represent the degree of structure of the fluid is the most logical approach as thixotropy is directly related to the structure of the blood. The structural parameter goes from zero to unity as the fluid goes from no structure at all to its maximally structured state. λ is subjected to a relaxation equation consisting of construction and destruction terms (see section 1.3.3). The construction term is usually based on Brownian motion and the destruction term on shear induced breakdown. In the MBM model (equation 1.31) and the model by Stephanou et al. (equation 1.34), the shear induced breakdown term is of the form $k\underline{\underline{\sigma}} : \underline{\underline{D}}$ or $k\underline{\underline{\nabla v}}^T : \underline{\underline{\tilde{c}}}$. They represent indeed a shear induced breakdown as they are approximately proportional to $\dot{\gamma}^2$ [13], but the presence of the logarithm in the λ -relaxation equation in the model by Stephanou et al. [33] forces λ asymptotically to very small values making the model non-linearity difficult to resolve numerically. When this happens, the

model is not able to converge. The approach followed in the HAWB model [13] tries to enforce that λ stays between zero and unity, by multiplying the shear induced breakdown term with λ . This results in a better conditioned system of equations. It also makes the construction term physically more correct by adding a shear induced construction term which is proportional to the shear rate. The general relaxation equation thus has the following form:

$$\frac{d}{dt}\lambda = \frac{1}{t_\lambda} \left((1 - \lambda) + (1 - \lambda)t_a|\dot{\gamma}| - \lambda(t_b\dot{\gamma})^2 \right) \quad (3.15)$$

Replacing the λ -equation in the Stephanou model creates an adapted model that is referred to as the modified Stephanou model. t_λ , t_a and t_b determine the shape and magnitude of the λ -curve. Figure 3.22 gives the structural parameter in function of the dimensionless radius with flow conditions according to the modified Stephanou model flow with $Wo = 0.23$ and $\frac{d\tilde{p}}{d\tilde{z}} = -7.9$. The figure was calculated using 6 harmonics and 11 Chebyshev nodes. In this figure, which is used as the reference case, $t_\lambda = 50$, $t_a = 0$ and $t_b = 0.5$.

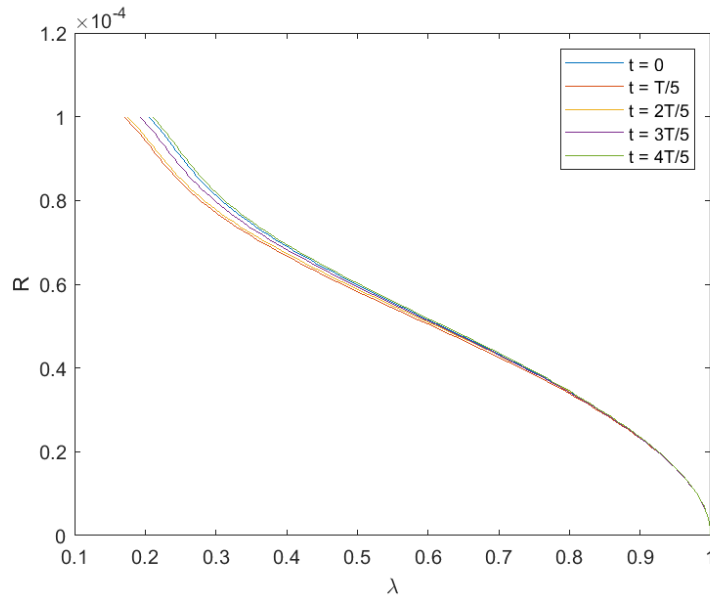


Figure 3.22: Radial profiles of the structure parameter for the modified Stephanou model subjected to pulsatile flow at 5 equidistant points in a period for $t_\lambda = 50$, $t_a = 0$, $t_b = 0.5$, $Wo = 0.23$ and $\frac{d\tilde{p}}{d\tilde{z}} = -7.9$.

In this case the structural parameter goes from approximately 0.3 to 1, which is a significant range. The shape of the structure equation also makes sense: it is lower at higher radii, where it is subjected to higher shear rates and 1 at the center-line where no shear is present. When t_λ is decreased, the structural parameter becomes more sensitive to changes in the shear rate, as is shown in Figure 3.23 where t_λ is reduce from 50 to 10.

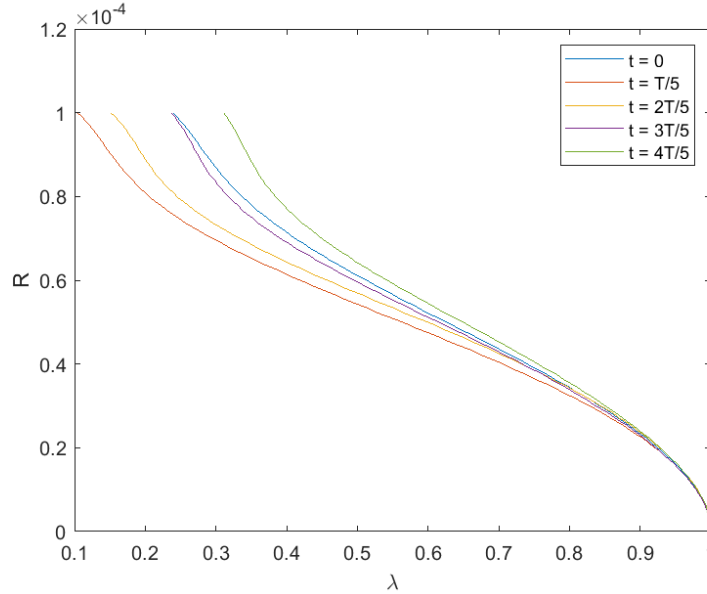


Figure 3.23: Radial profiles of the structure parameter for the modified Stephanou model subjected to pulsatile flow at 5 equidistant points in a period for $t_\lambda = 10$, $t_a = 0$, $t_b = 0.5$, $Wo = 0.23$ and $\frac{d\bar{p}}{dz} = -7.9$.

t_b mainly controls the magnitude of λ with varying radius as the shear induced breakdown term is proportional to the shear rate squared. Figure 3.24 shows a reduction from $t_b = 0.5$ to $t_b = 0.25$. The result is that the maximum value of λ increases from approximately 0.1 to 0.6. t_a increases the maximum magnitude of λ as well as making its profile more linear. Figure 3.25 shows an increase of t_a from 0 to 5.

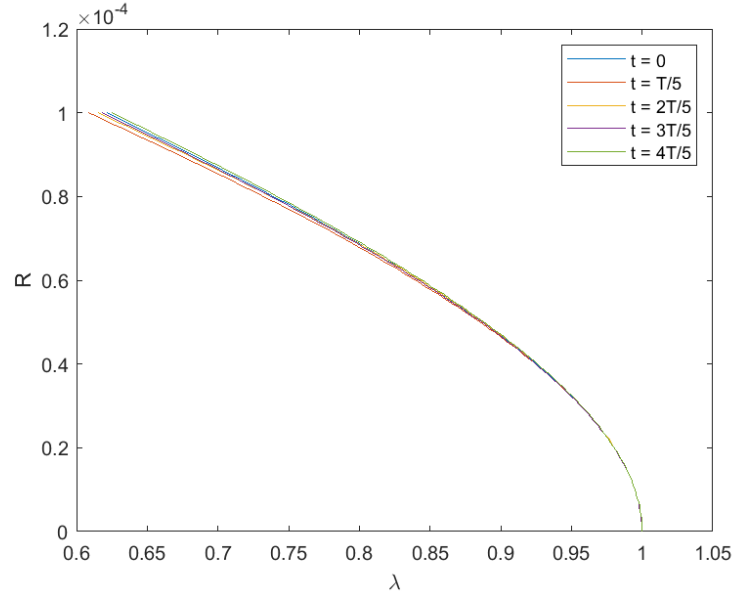


Figure 3.24: Radial profiles of the structure parameter for the modified Stephanou model subjected to pulsatile flow at 5 equidistant points in a period for $t_\lambda = 50$, $t_a = 0$, $t_b = 0.25$, $Wo = 0.23$ and $\frac{d\bar{p}}{d\bar{z}} = -7.9$.

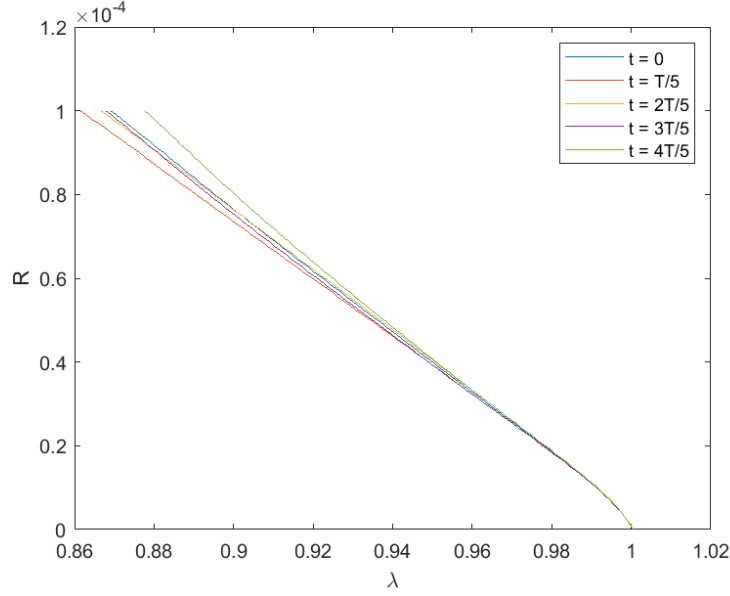


Figure 3.25: Radial profiles of the structure parameter for the modified Stephanou model subjected to pulsatile flow at 5 equidistant points in a period for $t_\lambda = 50$, $t_a = 5$, $t_b = 0.5$, $Wo = 0.23$ and $\frac{d\tilde{p}}{d\tilde{z}} = -7.9$.

3.2.2 Collocation Method for modified Stephanou model

Knowing that it makes sense to include a structural parameter in rheological models for Poiseuille flow, the Stephanou model [33] (see section 1.3.3) is used to calculate the velocity profile of blood, including shear thinning, viscoelasticity and thixotropy. To keep the number of equations as low as possible to make the Jacobian better conditioned, the equations regarding the normal stress components are disregarded because the normal stress difference is not relevant in calculating the velocity profile in a tubular vessel with rigid walls. For now the focus lies on the viscoelastic term of the Stephanou model. This term covers viscoelastic as well as thixotropic and shear thinning properties. The result is a model with 3 equations, which the author calls the modified Stephanou model. The equations are made dimensionless according to Table 2.1:

$$Wo^2 \frac{\partial \tilde{v}_z}{\partial \tilde{t}}(\tilde{r}, \tilde{t}) = -\frac{d\tilde{p}}{d\tilde{z}}(1 + \sin(\tilde{t})) + \frac{\tilde{\sigma}_{rz}}{\tilde{r}}(\tilde{r}, \tilde{t}) + \frac{\partial \tilde{\sigma}_{rz}}{\partial \tilde{r}}(\tilde{r}, \tilde{t}) \quad (3.16)$$

$$\begin{aligned}
Wo &= \sqrt{\frac{\rho\omega^2 R^2}{G}} \\
\tilde{t}_m \frac{\partial \tilde{\sigma}_{rz}}{\partial \tilde{t}} + (1 - \lambda)\tilde{\sigma}_{rz} &= \tilde{t}_m \tilde{\gamma} \\
\frac{\partial \lambda}{\partial \tilde{t}} &= \frac{1}{\tilde{t}_\lambda} \left((1 - \lambda) + (1 - \lambda)\tilde{t}_a |\tilde{\gamma}| - \lambda(\tilde{t}_b \tilde{\gamma})^2 \right) \\
\tilde{v}_z(1, \tilde{t}) = 0 \quad \tilde{\gamma}(0, \tilde{t}) = 0 \quad \tilde{v}_z(\tilde{r}, 0) &= \tilde{v}_z(\tilde{r}, 2\pi)
\end{aligned}$$

All the results in this section are calculated using 6 harmonics and 11 Chebyshev nodes, to make sure that the calculations are high accuracy. The lambda equation from the reference case is used, i.e. equation 3.15 with $t_\lambda = 50, t_a = 0, t_b = 0.5$. This is shown in Figure 3.22. These parameters are not based on experiments, but are designed to demonstrate the capabilities of the numerical algorithm. The parameters can be further refined in combination with experimental data. Appendix C shows the coefficients for all the Fourier and Chebyshev nodes of all the output variables. In the Vertical direction, the Fourier nodes are represented and in the Chebyshev nodes are shown in the horizontal direction, as explained in equation 2.8. In the limit the coefficients decrease approximately with one order of magnitude per node, both in the time and radial direction. Figure 3.26 shows the Lissajous plot in the shear stress - shear rate domain for 4 different radii for $G = 0.019$ and $t_m = 0.14$ as in the paper by Stephanou et al. [33]. The ellipses become wider towards the centerline, meaning that the flow becomes more elastic at the centerline and more viscous at the border. The fact that the ellipses differ with the radius indicates thixotropy. Going closer to the edge of the tubular vessel, the ellipses span less of the domain from -1 to 1, indicating more shear thinning towards the edge.

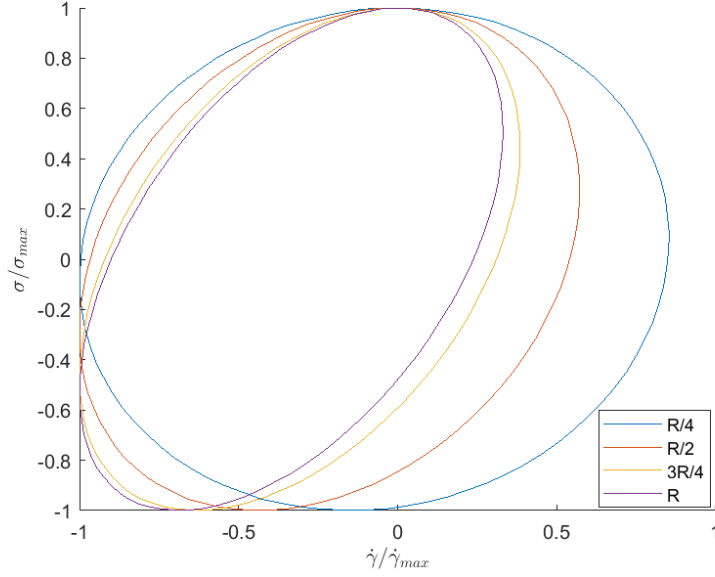


Figure 3.26: Lissajous plot in the shear stress - shear rate domain for the viscoelastic part of the modified Stephanou model subjected to pulsatile flow for $t_\lambda = 50, t_a = 0, t_b = 0.5, G = 0.019$ and $\frac{d\tilde{p}}{dz} = -7.9$.

Figure 3.27 shows the shear rate profile. It is clearly more non-linear compared to the viscoelastic shear rate profile in Figure 3.13. Towards the edge, the absolute value of the shear rate decreases again. The current explanation for this is that both viscoelasticity and shear thinning increase the shear rate towards the edge of the tubular vessel, but to a different extent. For this set of parameters the viscoelasticity increases the shear rate more than the shear thinning behavior increases the shear rate. The structural parameter λ also decreases towards the edge and determines whether viscoelasticity or shear thinning dominates. At a certain radius λ becomes small enough that the dominance shifts towards the viscous, shear thinning characteristics. This can also be seen in figure 3.28, where the magnitude of the shear rate is shown for $r = R$ and $r = 0.95R$. The figure shows a crossover of the two profiles explaining the hooking behavior that is seen in Figure 3.27. However, this calculation does not account for the RBC depletion layer towards the edge and for the viscous contribution of the blood plasma. So, experiments need

to be carried out to further explain this phenomena and test whether it exists for actual flow conditions in the body.

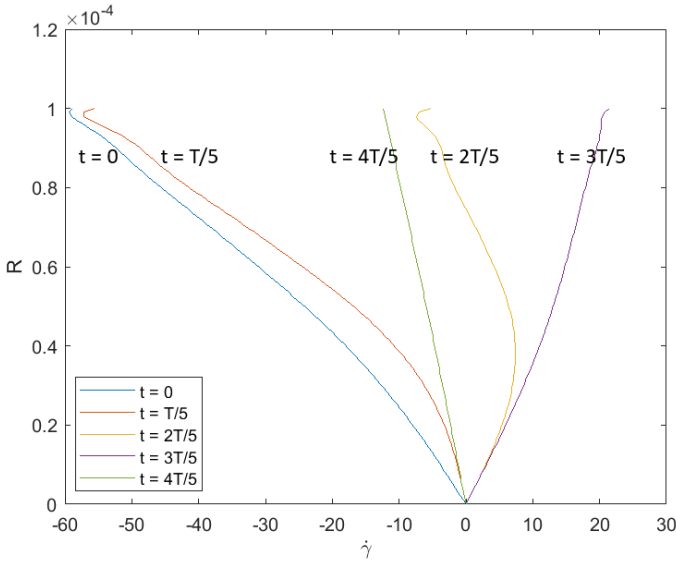


Figure 3.27: Shear rate for 5 equidistant time points in the periodic domain for the viscoelastic part of the modified Stephanou model subjected to pulsatile flow for $t_\lambda = 50, t_a = 0, t_b = 0.5, G = 0.019$ and $\frac{d\bar{p}}{d\bar{z}} = -7.9$.

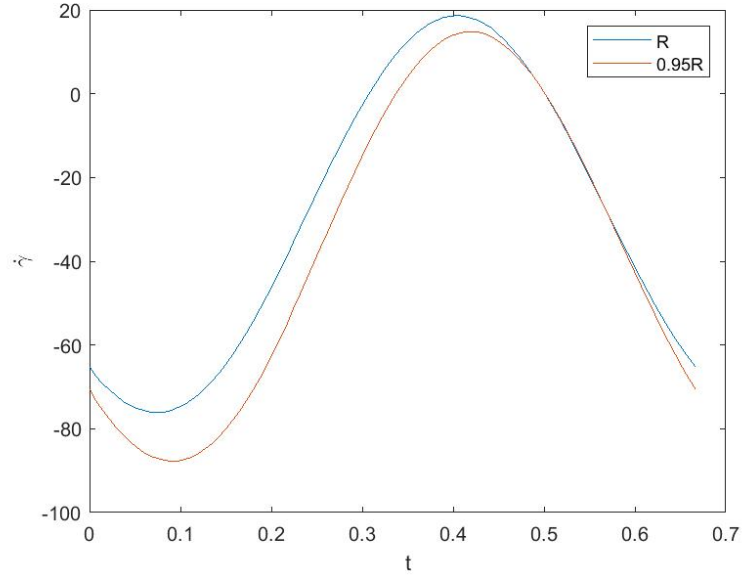


Figure 3.28: Shear rate for $r = R$ and $r = 0.95R$ for the viscoelastic part of the modified Stephanou model subjected to pulsatile flow for $t_\lambda = 50, t_a = 0, t_b = 0.5, G = 0.019$ and $\frac{d\bar{p}}{d\bar{z}} = -7.9$.

The shear stress in Figure 3.29 does not differ much from the purely viscoelastic case in Figure 3.14, except for the magnitude, because of the smaller Womersley ($Wo = 0.23$) number in the calculation of the Stephanou model.

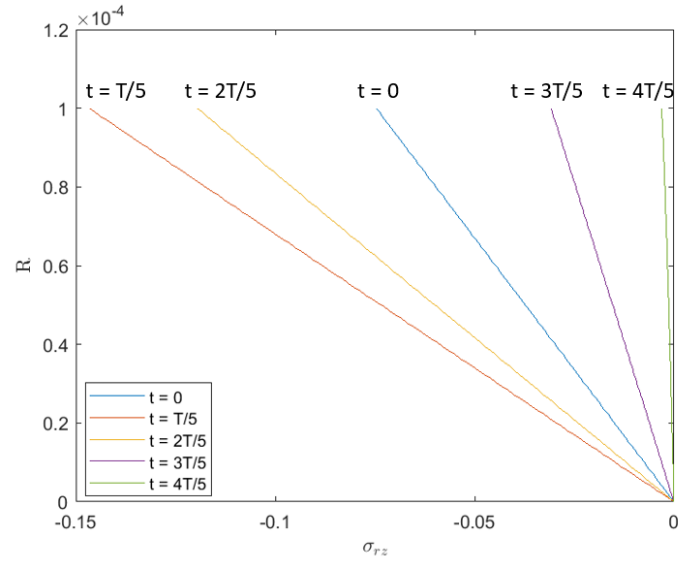


Figure 3.29: Shear stress for 5 equidistant time points in the periodic domain for the viscoelastic part of the modified Stephanou model subjected to pulsatile flow for $t_\lambda = 50, t_a = 0, t_b = 0.5, G = 0.019$ and $\frac{d\bar{p}}{dz} = -7.9$.

The velocity profile in Figure 3.30 looks more non-linear than the velocity profile for the Maxwell fluid in Figure 3.12. A phase shift is also observed when comparing the two figures, with the maximum now occurring at $t = 0$ instead of $t = T/5$.

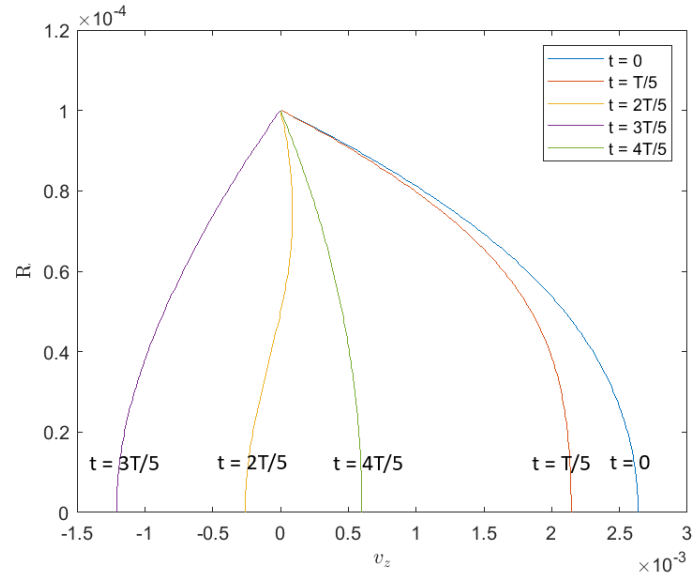


Figure 3.30: Axial velocity for 5 equidistant time points in the periodic domain for the viscoelastic part of the modified Stephanou model subjected to pulsatile flow for $t_\lambda = 50, t_a = 0, t_b = 0.5, G = 0.019$ and $\frac{d\bar{p}}{d\bar{z}} = -7.9$.

Chapter 4

CONCLUSIONS AND FUTURE WORK

Blood is a complex fluid showing shear thinning, viscoelastic and thixotropic effects. These effects are important to investigate because is subjected to the pulsating flow conditions in our body. The study of blood rheology can aid in the diagnosis of blood related diseases in combination with already existing blood research tools. The flow conditions are best represented with UD-LAOS flow, but with the pressure gradient being the driving force instead of the shear. A lot of research has been done considering UD-LAOS flow, but this thesis is one of the first works to focus on pulsatile Poiseuille flow by developing a mathematical algorithm that computes blood flow efficiently under these conditions. This is done by taking advantage of the mathematical form of the flow conditions and the cylindrical geometry. The model works according to a collocation method, where orthogonal Fourier and Chebyshev polynomials are fitted to the solutions. This makes the solution semi-analytic and introduces only an interpolation error on top of the machine error.

The model was successfully validated for the calculation of Newtonian fluids, elastic solid, Maxwellian fluids and power law fluids, whilst also showing the capability to solve more complicated models including a structural parameter. This was demonstrated for the model developed by Stephanou et al. [33] The algorithm is able to reach much higher accuracies than finite difference methods whilst solving for much less unknowns, making it also faster. The interpolation error decreases very fast when using higher order polynomials but increases again when using

polynomials of too high order. The biggest weakness of the model is that the Jacobian is often poorly conditioned. Suggested ways to improve the condition number are constructing using adapted time and radial matrices that automatically fit the initial and boundary conditions of the problem, or to adapt the code to make it possible to choose the amount of Fourier and Chebyshev nodes separately for each output variable. Also reducing the amount of different output variables to the minimum amount possible helps. Another disadvantage of the model is that is only applicable to one specific geometry and does not include entrance effects and syneresis effects at the wall.

The most important contribution of this work is the development of an efficient code, that is able to solve complex blood flow models. This can be a great aid in defining new rheological models more suited for pulsating Poiseuille flow in the future, coming one step closer to modelling the flow conditions in the human body. The model is meant to use in combination with a microfluidic device that acts under the same flow conditions. The collaboration between experiments and modelling is very important. The experiments can help to come up with better conditioned models and better adapted parameters for pulsating Poiseuille flow. The model can help to understand the underlying physics and to make realistic predictions for other flow parameters. This opens the path to a new method of researching blood rheology in a way that more closely resembles the flow conditions in the human body.

BIBLIOGRAPHY

- [1] P. M. Ness and J. M. Stengle. *The red blood cell - a comprehensive treatise*, volume 1, chapter 1, pages 1–50. Academic press, New York, 2nd edition, 1974.
- [2] F. P. Incropera, D. P. Dewitt, T. L. Bergman, and A. S. Lavine. *Fundamentals of Heat and Mass Transfer*. John Wiley and Sons, 6th edition, 2006.
- [3] C. Nordqvist. Blood: Everything you need to know today. *Medical News Today*.
- [4] A. J. Vander, J. H. Sherman, and D. S. Luciano. *Human Physiology: The Mechanisms of Body Function*. McGraw-Hill, 6th edition, 1994.
- [5] G. P. Galdi, R. Rannacher, A. M. Robertson, and S. Turek. *Hemodynamical Flows: Modeling, Analysis and Simulation*. Birkhuser, 2008.
- [6] M. Thiriet. *Biology and Mechanics of Blood Flows*, volume 2. Springer-Verlag, 2008.
- [7] S. Chien. *The red blood cell - a comprehensive treatise*, volume 2, chapter 1, pages 1031–1131. Academic press, New York, 2 edition, 1975.
- [8] D. A. Fedosov, B. Caswell W. Pan, G. Gompper, and G. E. Karniadakis. Predicting human blood viscosity in silico. *PNAS USA*, 108:11772–11777, 2011.
- [9] D. E. Brooks. The effect of neutral polymers on the electrokinetic potential of cells and other charged particles iii. experimental studies on the dextran/erythrocyte system. *Journal of Colloid Interface Science*, 43:700–713, 1973.
- [10] E. W. Merrill, E. R. Gilliland, T. S. Lee, and E. W. Salzman. Blood rheology: Effect of fibrinogen deduced by addition. *Circulation Research*, 18:437–446, 1966.
- [11] S. Chien and K. Jan. Ultrastructural basis of the mechanism of rouleaux formation. *Microvascular Research*, 5:155–166, 1973.
- [12] R. D. Guy, A. L. Fogelson, and J. P. Keener. Fibrin formation in a shear flow. *Math. Med. Biol.*, 24:111–130, 2007.
- [13] J. S. Horner, M. J. Armstrong, N. J. Wagner, and A. N. Beris. Investigation of blood rheology under steady and unidirectional large amplitude oscillatory shear. *Journal of Rheology*, 62:577–591, 2018.

- [14] S. Asakura and F. Oosawa. On interaction between two bodies immersed in a solution of macromolecules. *Journal of Chemical Physics*, 22:1255–1256, 1954.
- [15] H. Baumler, B. Neu, E. Donath, and H. Kieseewetter. Basic phenomena of red blood cell rouleaux formation. *Biorheology*, 36:439–442, 1999.
- [16] J. K. Armstrong, R. B. Wenby, H. J. Meiselman, and T. C. Fisher. The hydrodynamic radii of macromolecules and their effect on red blood cell aggregation. *Journal of Biophysics*, 87:4259–4270, 2004.
- [17] M. W. Johnson and D. Segalman. A model for viscoelastic fluid behavior which allows non-affine deformation. *Journal of Non-Newtonian Fluid Mechanics*, 2:255–270, 1977.
- [18] M. Puig-De-Morales-Marinkovic et al. Viscoelasticity of the human red blood cell. *American Journal of Physiology-Cell Physiology*, 293:C597–C605, 2007.
- [19] E. E. Herrera-Valencia et al. On the pulsating flow behavior of a biological fluid: human blood. *Rheologica Acta*, 56:387–407, 2017.
- [20] A. Siginer. Oscillating flow of a simple fluid in a pipe. *International Journal of Engineering Science*, 29:1557–1567, 1991.
- [21] O. Manero and K. Walters. On elastic effects in unsteady pipe flows. *Rheologica Acta*, 19:277–284, 1980.
- [22] S. E. Spagnolie. *Complex Fluids in Biological Systems*, volume 1, chapter 11, pages 399–435. Springer-Verlag, New York, 1st edition, 2014.
- [23] Y. C. Fung. *Biodynamics: Circulation*. Springer, 1996.
- [24] R. Skalak, N. Ozkaya, and T. C. Skalak. Biofluid mechanics. *Annual Review of Fluid Mechanics*, 21:167–200, 1989.
- [25] S. Kim et al. The cell-free layer in microvascular blood flow. *Biorheology*, 46(3):181–189, 2009.
- [26] A. Pries, D. Neuhaus, and P. Gaehtgens. Blood viscosity in tube flow: dependence on diameter and hematocrit. *American Journal of Physiology*, 263(6):H1170–H1178, 1992.
- [27] J. Ho, W. J. Sibbald, and I. H. Chin-Yee. Effects of storage on efficacy of red cell transfusion: When is it not safe? *Critical Care Medicine*, 31:s687–s697, 2003.
- [28] M. Uyuklu et al. Effects of storage duration and temperature of human blood on red cell deformability and aggregation. *Clinical Hemorheology and Microcirculation*, 41:269–278, 2009.

- [29] J. Mewis and N. J. Wagner. *Colloidal Suspension Rheology*. Cambridge University press, 2012.
- [30] A. J. Apostolidis, M. J. Armstrong, and A. N. Beris. Modeling of human blood rheology in transient shear flows. *Journal of Rheology*, 59:275–298, 2015.
- [31] J. G. Oldroyd. On the formulation of rheological equations of state. *Proceedings of the Royal Society*, A200:523–541, 1950.
- [32] A. N. Beris and B. J. Edwards. *Thermodynamics of Flowing Systems with Internal Microstructure*. Oxford University Press, 1994.
- [33] P. S. Stephanou and G. G. Georgiou. A nonequilibrium thermodynamics perspective of thixotropy. *Journal of Chemical Physics*, 149:244902, 2018.
- [34] M. Anand, J. Kwack, and A. Masud. A new generalized oldroyd-b model for blood flow in complex geometries. *International Journal of Engineering Science*, 72:78–88, 2013.
- [35] S. Tabatabaei et al. Modified bautista-manero (mbm) modelling for hyperbolic contraction-expansion flows. *Rheologica Acta*, 54:869–885, 2015.
- [36] J. R. Casterjn-Pita, J. A. del Rio, A. A. Casterjn-Pita, and G. Huelsz. Experimental observation of dramatic differences in the dynamic response of newtonian and maxwellian fluids. *Physical Review*, 68:046301, 2003.
- [37] A. F. Stalder et al. Assessment of flow instabilities in the healthy aorta using flow-sensitive mri. *Journal of magnetic resonance imaging*, 33:839–846, 2011.
- [38] A. Bultheel, K. Meerbergen, and D. Roose. *Numerieke wiskunde*. Acco, 2010.
- [39] T. Kenner. The measurement of blood density and its meaning. *Basic research in Cardiology*, 84:111–124, 1989.
- [40] Z.Chen, U. Gandhi, J.Lee, and R. H. Wagoner. Variation and consistency of young's modulus in steel. *Journal of Materials Processing Technology*, 227:227–243, 2016.
- [41] R. B. Bird, W. E. Stewart, and E. N. Lightfoot. *Transport Phenomena*. John Wiley and Sons, 2nd edition.

Appendix A
REPRINT PERMISSION LETTERS

This appendix contains the letters necessary to reprint figures that have been published in papers.

**AIP PUBLISHING LICENSE
TERMS AND CONDITIONS**

Apr 16, 2019

This Agreement between Tim Van de Vyver ("You") and AIP Publishing ("AIP Publishing") consists of your license details and the terms and conditions provided by AIP Publishing and Copyright Clearance Center.

License Number	4570820628309
License date	Apr 16, 2019
Licensed Content Publisher	AIP Publishing
Licensed Content Publication	Journal of Rheology
Licensed Content Title	Investigation of blood rheology under steady and unidirectional large amplitude oscillatory shear
Licensed Content Author	Jeffrey S. Horner, Matthew J. Armstrong, Norman J. Wagner, et al
Licensed Content Date	Mar 1, 2018
Licensed Content Volume	62
Licensed Content Issue	2
Type of Use	Thesis/Dissertation
Requestor type	Student
Format	Print and electronic
Portion	Figure/Table
Number of figures/tables	2
Title of your thesis / dissertation	Development of a numerical model for blood rheology subjected to pulsating Poiseuille flow in a cylindrical vessel
Expected completion date	Apr 2019
Estimated size (number of pages)	80
Requestor Location	Tim Van de Vyver 411 Hamlet Way NEWARK, DE 19711 United States Attn: Tim Van de Vyver
Total	0.00 USD

Terms and Conditions

The Society of Rheology -- Terms and Conditions: Permissions Uses

The Society of Rheology ("SOR") hereby grants to you the non-exclusive right and license to use and/or distribute the Material according to the use specified in your order, on a one-time basis, for the specified term, with a maximum distribution equal to the number that you have ordered. Any links or other content accompanying the Material are not the subject of this license.

1. You agree to include the following copyright and permission notice with the reproduction of the Material: "Reprinted with permission from [FULL CITATION]. Copyright [PUBLICATION YEAR], The Society of Rheology." For an article, the copyright and permission notice must be printed on the first page of the article or book chapter. For photographs, covers, or tables, the copyright and permission notice may appear with the Material, in a footnote, or in the reference list.
2. If you have licensed reuse of a figure, photograph, cover, or table, it is your responsibility to ensure that the material is original to SOR and does not contain the copyright of another entity, and that the copyright notice of the figure, photograph, cover, or table does not

indicate that it was reprinted by SOR, with permission, from another source. Under no circumstances does SOR, purport or intend to grant permission to reuse material to which it does not hold copyright.

3. You may not alter or modify the Material in any manner. You may translate the Material into another language only if you have licensed translation rights. You may not use the Material for promotional purposes. SOR reserves all rights not specifically granted herein.
4. The foregoing license shall not take effect unless and until SOR or its agent, Copyright Clearance Center, receives the Payment in accordance with Copyright Clearance Center Billing and Payment Terms and Conditions, which are incorporated herein by reference.
5. SOR or the Copyright Clearance Center may, within two business days of granting this license, revoke the license for any reason whatsoever, with a full refund payable to you. Should you violate the terms of this license at any time, SOR, The Society of Rheology, or Copyright Clearance Center may revoke the license with no refund to you. Notice of such revocation will be made using the contact information provided by you. Failure to receive such notice will not nullify the revocation.
6. SOR makes no representations or warranties with respect to the Material. You agree to indemnify and hold harmless SOR, The Society of Rheology, and their officers, directors, employees or agents from and against any and all claims arising out of your use of the Material other than as specifically authorized herein.
7. The permission granted herein is personal to you and is not transferable or assignable without the prior written permission of SOR. This license may not be amended except in a writing signed by the party to be charged.
8. If purchase orders, acknowledgments or check endorsements are issued on any forms containing terms and conditions which are inconsistent with these provisions, such inconsistent terms and conditions shall be of no force and effect. This document, including the CCC Billing and Payment Terms and Conditions, shall be the entire agreement between the parties relating to the subject matter hereof.

This Agreement shall be governed by and construed in accordance with the laws of the State of New York. Both parties hereby submit to the jurisdiction of the courts of New York County for purposes of resolving any disputes that may arise hereunder.

Questions? customer@copyright.com or +1-855-239-3415 (toll free in the US) or +1-978-646-2777.

Appendix B

ELASTIC LIMIT OF THE MAXWELL FLUID

The velocity expression for a fluid subjected to a pulsating pressure drop with one harmonic is:

$$v(r, \omega) = \Re \left[\left(\frac{R^2}{4\eta} \left(1 - \left(\frac{r}{R} \right)^2 \right) + \frac{1 - i\omega t_m}{\eta\beta^2} \left(1 - \frac{J_0(\beta r)}{J_0(\beta R)} \right) \sin(t) \right) \frac{dp}{dz} \right] \quad (\text{B.1})$$

$$\beta = \sqrt{\frac{\rho((\omega t_m)^2 + i\omega t_m)}{\eta t_m}}$$

$t_m = \eta/G$ goes to infinity, meaning that η goes to infinity because G does not go to zero. If η goes to infinity, the first term in the above velocity expression goes to zero.

Then for the second term:

$$\begin{aligned} \lim_{t_m, \eta \rightarrow \infty} \left[\frac{1 - i\omega t_m}{\eta\beta^2} \right] &= \lim_{t_m, \eta \rightarrow \infty} \left[\frac{(1 - i\omega t_m)t_m}{\rho((\omega t_m)^2 + i\omega t_m)} \right] \\ &= \lim_{t_m, \eta \rightarrow \infty} \left[\frac{(1 - i\omega t_m)}{\rho(\omega^2 t_m + i\omega)} \frac{(\omega^2 t_m - i\omega)}{(\omega^2 t_m - i\omega)} \right] \\ &= \lim_{t_m, \eta \rightarrow \infty} \left[\frac{(\omega^2 t_m - i\omega - i\omega^3 t_m^2 - \omega^2 t_m)}{\rho(\omega^4 t_m^2 + \omega^2)} \right] \\ &= \lim_{t_m, \eta \rightarrow \infty} \left[\frac{(-i(\omega + \omega^3 t_m^2))}{\rho(\omega^4 t_m^2 + \omega^2)} \right] \\ &= \lim_{t_m, \eta \rightarrow \infty} \left[\frac{-i}{\rho\omega} \right] \end{aligned} \quad (\text{B.2})$$

$$\begin{aligned} \lim_{t_m \rightarrow \infty} [\beta] &= \lim_{t_m \rightarrow \infty} \left[\sqrt{\frac{\rho((\omega t_m)^2 + i\omega t_m)}{G t_m^2}} \right] \\ &= \left[\sqrt{\frac{\rho\omega^2}{G}} \right] \end{aligned} \quad (\text{B.3})$$

This gives as final result:

$$v(r, \omega) = \Re \left[\frac{-i}{\rho\omega} \left(1 - \frac{J_0(\beta r)}{J_0(\beta R)} \right) \frac{dp}{dz} \sin(t) \right] \quad (\text{B.4})$$

$$\beta = \sqrt{\frac{\rho}{G}} \omega$$

Appendix C

TABLES

This appendix includes the node coefficients for the structural parameter, the displacement and the shear stress respectively for the Stephanou model, calculated with 6 Fourier nodes and 11 Chebyshev nodes.

Table C.1: Structural parameter node coefficients

-5.5E+02	1.0E+03	-8.6E+02	6.3E+02	4.0E+02	2.2E+02	-1.0E+02	3.8E+01	-1.1E+01	2.2E+00	-2.4E-01
-2.0E+01	3.8E+01	-3.1E+01	2.3E+01	-1.5E+01	8.0E+00	-3.7E+00	1.4E+00	-4.2E-01	8.9E-02	-1.0E-02
2.5E+01	-4.8E+01	4.0E+01	-2.9E+01	1.8E+01	-9.8E+00	4.5E+00	-1.7E+00	4.8E-01	-9.5E-02	9.8E-03
8.1E+00	-1.5E+01	1.2E+01	-9.0E+00	5.7E+00	-3.1E+00	1.4E+00	-5.1E-01	1.5E-01	-2.8E-02	2.9E-03
4.9E+00	-9.3E+00	7.7E+00	-5.6E+00	3.6E+00	-2.0E+00	9.2E-01	-3.5E-01	1.1E-01	-2.3E-02	2.6E-03
-1.5E-02	2.7E-02	-1.9E-02	9.5E-03	-1.9E-03	-2.1E-03	2.9E-03	-2.1E-03	9.8E-04	-3.1E-04	5.0E-05
-6.0E-01	1.1E+00	-9.3E-01	6.7E-01	-4.3E-01	2.3E-01	-1.1E-01	3.9E-02	-1.1E-02	2.3E-03	-2.4E-04
-1.0E-01	1.9E-01	-1.6E-01	1.1E-01	-7.1E-02	3.9E-02	-1.8E-02	6.6E-03	-1.9E-03	3.8E-04	-3.9E-05
3.6E-03	-6.5E-03	4.8E-03	-2.7E-03	1.0E-03	-3.4E-05	-3.1E-04	2.8E-04	-1.5E-04	4.9E-05	-8.1E-06
3.7E-03	-7.0E-03	5.8E-03	-4.1E-03	2.6E-03	-1.4E-03	6.1E-04	-2.2E-04	5.9E-05	-1.1E-05	9.9E-07
5.9E-03	-1.1E-02	9.1E-03	-6.6E-03	4.2E-03	-2.3E-03	1.1E-03	-4.0E-04	1.2E-04	-2.4E-05	2.6E-06
6.5E-04	-1.2E-03	1.0E-03	-7.3E-04	4.6E-04	-2.5E-04	1.2E-04	-4.4E-05	1.3E-05	-2.6E-06	2.9E-07
-4.1E-04	7.8E-04	-6.4E-04	4.6E-04	-2.8E-04	1.5E-04	-6.6E-05	2.4E-05	-6.3E-06	1.1E-06	-9.8E-08

Table C.2: Z node coefficients

1.1E+00	1.9E-01	-4.9E-02	-7.0E-04	-8.7E-03	-9.6E-03	-7.7E-03	-5.1E-03	-2.6E-03	-7.9E-04	-1.2E-04
2.0E+00	-7.0E-03	1.1E-03	2.5E-04	1.5E-04	2.8E-04	2.2E-04	1.4E-04	7.3E-05	2.3E-05	3.4E-06
-1.1E+00	-1.9E-01	5.0E-02	5.0E-04	8.8E-03	9.7E-03	7.7E-03	5.1E-03	2.6E-03	7.9E-04	1.2E-04
-9.2E-03	-1.7E-03	4.4E-04	-1.1E-04	-6.7E-05	-3.2E-05	-4.7E-05	-2.7E-05	-1.3E-05	-4.8E-06	-9.4E-07
1.1E-03	8.1E-04	-1.6E-04	-1.0E-04	-1.5E-05	-6.3E-05	-4.6E-05	-2.8E-05	-1.6E-05	-5.1E-06	-7.5E-07
-7.2E-04	5.0E-08	1.0E-05	-1.6E-05	4.7E-06	-3.2E-06	-1.7E-06	-7.9E-07	-6.4E-07	-2.5E-07	-3.2E-08
9.6E-04	1.2E-04	-5.8E-05	1.3E-05	5.6E-06	1.7E-06	3.9E-06	2.1E-06	1.0E-06	4.2E-07	9.1E-08
-3.2E-05	-1.7E-05	-1.9E-06	2.3E-07	-5.6E-07	-5.6E-07	-4.0E-07	-2.9E-07	-1.3E-07	-3.4E-08	-4.1E-09
-1.8E-05	-3.6E-06	1.3E-06	2.4E-07	1.9E-07	4.3E-07	3.1E-07	1.9E-07	1.1E-07	3.2E-08	4.0E-09
-3.2E-06	-9.7E-07	7.1E-08	5.6E-08	3.8E-08	6.3E-08	4.9E-08	3.1E-08	1.6E-08	5.0E-09	6.5E-10
5.3E-07	7.1E-07	9.4E-08	-3.4E-08	4.5E-08	4.6E-08	3.0E-08	2.3E-08	1.0E-08	2.2E-09	2.2E-10
7.2E-08	-1.1E-08	-1.6E-08	-3.4E-09	-1.6E-10	-1.3E-09	-1.2E-09	-6.3E-10	-4.1E-10	-1.8E-10	-3.3E-11
-1.1E-07	-6.0E-08	-1.1E-08	-8.9E-10	-3.5E-09	-4.2E-09	-3.1E-09	-2.1E-09	-1.1E-09	-3.0E-10	-3.4E-11

Table C.3: σ_{yz} node coefficients

-3.9E+00	-5.8E-15	-1.3E-14	-3.2E-14	-6.3E-14	-9.0E-14	-7.5E-14	-3.8E-15	6.5E-14	6.4E-14	2.1E-14
-4.0E+00	1.4E-02	-2.3E-05	4.0E-07	7.6E-07	-1.5E-07	-7.3E-09	8.0E-09	-3.4E-08	-1.8E-08	-4.0E-09
2.0E-02	-4.8E-03	-8.9E-04	1.2E-04	-3.8E-06	-8.7E-07	2.3E-07	-2.1E-07	-1.2E-06	-5.6E-07	-1.4E-07
6.7E-04	-1.5E-04	-3.4E-05	3.6E-06	6.4E-07	-5.6E-07	1.3E-07	4.0E-09	2.1E-08	2.2E-08	8.3E-09
-4.7E-05	-1.2E-05	7.9E-06	2.1E-06	-1.3E-06	2.4E-07	1.5E-08	-1.8E-08	3.1E-08	1.8E-08	3.4E-09
1.4E-04	-4.2E-05	-2.9E-06	1.6E-06	-5.7E-07	9.7E-08	6.8E-09	-9.5E-09	3.9E-09	2.6E-09	1.4E-10
-1.7E-04	4.0E-05	7.6E-06	-1.2E-06	-1.4E-07	1.5E-07	-3.8E-08	8.4E-10	-3.5E-09	-5.4E-09	-2.1E-09
6.9E-06	-8.0E-07	-3.2E-07	-1.1E-07	8.6E-09	5.5E-09	-3.0E-09	9.9E-10	9.4E-10	6.2E-11	1.8E-11
5.2E-06	-1.1E-06	-2.6E-07	5.8E-09	2.0E-08	-5.3E-09	-5.6E-10	7.1E-10	-9.0E-10	-3.2E-10	-1.7E-11
1.4E-06	-2.7E-07	-5.8E-08	-4.7E-09	3.7E-09	-6.7E-10	-1.6E-10	1.1E-10	-2.0E-10	-8.2E-11	-9.2E-12
-3.8E-08	-7.0E-08	7.6E-09	1.4E-08	-1.3E-09	-1.1E-09	5.3E-10	-1.6E-10	-1.1E-10	2.0E-11	5.1E-12
-5.8E-08	1.6E-08	2.3E-09	-9.5E-11	-3.1E-10	-4.4E-13	2.6E-11	-9.6E-12	6.6E-12	9.8E-12	2.2E-12
5.4E-08	-8.4E-09	-1.5E-09	-9.0E-10	-7.4E-11	6.9E-11	-1.1E-11	4.3E-13	1.7E-11	4.9E-12	-2.8E-13

Appendix D

MATLAB CODE

This appendix contains the Matlab code for the collocation method. It consists of a main file, which calls additional functions, like Newton's method and the Jacobian calculation file. Further the equation files for some equations are included: Newtonian, Maxwell, Carreau and Stephanou.

```

%Main file
clear all;clc;close all;

%control parameters
%%%%%%%%%%%%%%%%%%%%%%%%%%%%%%%%%%%%%%%%%%%%%%%%%%%%%%%%%%%%%%%%%%%%%%%%
omega = 90/60*2*pi; %angular velocity
amplitude = 1; %amplitude
n = 1; %number of harmonics included (number of Fourier nodes)
m = 7; %number of Chebyshev nodes
q = 2; %number of indepent outputs (dependent on model)
totalv = (2*n+1)*m*q;
equations = @ftVDV14M; %function with the equations (different function
                    %file for different model)
Jacobian = @dfdxTVDV14; %function with as output the Jacobian of the
                    %equation
%%%%%%%%%%%%%%%%%%%%%%%%%%%%%%%%%%%%%%%%%%%%%%%%%%%%%%%%%%%%%%%%%%%%%%%%

%Initialize values with dimensions
%%%%%%%%%%%%%%%%%%%%%%%%%%%%%%%%%%%%%%%%%%%%%%%%%%%%%%%%%%%%%%%%%%%%%%%%
P = -50; %pressure drop of the entire tube length
L = 2*10^(-3); %tube length
R0 = 10^(-4); %tube Radius
Hct = 0.42; %Blood Hematocrit to determine viscosity and yield stress
np0 = 1.67*10^(-3); %plasma viscosity
T0 = 296.16; %Reference temperature
Te = T0; %Temperature
%eta = np0*(1+2.0703*Hct+3.7222*Hct^2)*exp(-7.0276*(1-T0/Te)); %Viscosity
                    %according do Casson fit

eta = 1.25*10^(-3); %Viscosity
rho = 1200; %Density
T = 2*pi/omega; %period
deltat = T/(2*n+1); %timestep
t = 0:deltat:T-deltat; %time vector
tm = 1.9; %Characteristic material time
G = 0.019; %elastic modulus Stephanou model
tr = 0.014; %Tule parameters Stephanou model
tl = 0.14;
tlambda = 1960; %Time parameters structural equation
ta = 483;
tb = 10;
%Add more model specific parameters if needed
%%%%%%%%%%%%%%%%%%%%%%%%%%%%%%%%%%%%%%%%%%%%%%%%%%%%%%%%%%%%%%%%%%%%%%%%

%Initialize dimensionless values
%%%%%%%%%%%%%%%%%%%%%%%%%%%%%%%%%%%%%%%%%%%%%%%%%%%%%%%%%%%%%%%%%%%%%%%%
r = chebyshev_coefficients(0,1,m)';%dimensionless radius
rb = sqrt(0.5); %coordinate transformation
c = (0.25-rb^2)/(0.75*rb^2); %coordinate transformation for non-linear
                    %models
r = sqrt((c+1).*r.^2./(c.*r.^2+1)); %coordinate transformation for
                    %non-linear models

t = t'*omega; %dimensionless time
T = 2*pi; %dimensionless period
tm = tm*omega; %dimensionless Maxwell time
pbar = (P/L)/(eta*omega/R0); %dimensionless pressure gradient
Wo = sqrt(rho*omega*R0^2/eta); %Womersley number
p = 1; %exponent Carreau model
eta0 = 10; %Carreau model zero shear viscosity
G = G/(eta*omega); %Dimensionless model parameters

```

```

tr = tr*omega;
tl = tl*omega;
tlambda = tlambda*omega;
ta = ta*omega;
tb = tb*omega;
kc = 0.14;
kd = 0.14;
%Add more specific dimensionless model parameters if needed
%%%%%%%%%%%%%%%%%%%%%%%%%%%%%%%%%%%%%%%%%%%%%%%%%%%%%%%%%%%%%%%%%%%%%%%%

%Introduce time dependent matrix A and its first and second derivative A1
%and A2 respectively
%%%%%%%%%%%%%%%%%%%%%%%%%%%%%%%%%%%%%%%%%%%%%%%%%%%%%%%%%%%%%%%%%%%%%%%%
A = zeros(2*n+1);
A(:,1) = ones(2*n+1,1);
j = 1;
for i = 2:2:2*n+1
    A(:,i) = sin(j.*t);
    j = j+1;
end
j = 1;
for i = 3:2:2*n+1
    A(:,i) = cos(j.*t);
    j = j + 1;
end

A1 = zeros(2*n+1);
A1(:,1) = zeros(2*n+1,1);
j = 1;
for i = 2:2:2*n+1
    A1(:,i) = j.*cos(j.*t);
    j = j+1;
end
j = 1;
for i = 3:2:2*n+1
    A1(:,i) = -j.*sin(j.*t);
    j = j + 1;
end

A2 = zeros(2*n+1);
A2(:,1) = zeros(2*n+1,1);
j = 1;
for i = 2:2:2*n+1
    A2(:,i) = -j.^2.*sin(j.*t);
    j = j+1;
end
j = 1;
for i = 3:2:2*n+1
    A2(:,i) = -j.^2.*cos(j.*t);
    j = j + 1;
end

Az = A;
Az(:,1) = t;
A1z = A1;
A1z(:,1) = ones(2*n+1,1);
%%%%%%%%%%%%%%%%%%%%%%%%%%%%%%%%%%%%%%%%%%%%%%%%%%%%%%%%%%%%%%%%%%%%%%%%

%Introduce radial matrix B and its first and second derivative B1 and B2
%respectively

```

```

%%%%%%%%%%%%%%%%%%%%%%%%%%%%%%%%%%%%%%%%%%%%%%%%%%%%%%%%%%%%%%%%%%%%%%%%
Bd = zeros(2*m-1,m); %Matrix used to prepare even B matrix
Bd(1,:) = ones(1,m);
Bd(2,:) = r;
for i = 3:2*m-1
    Bd(i,:) = 2.*r.*Bd(i-1,)-Bd(i-2,:);
end
Bd1 = zeros(2*m-1,m);
Bd1(1,:) = zeros(1,m);
Bd1(2,:) = ones(1,m);
for i = 3:2*m-1
    Bd1(i,:) = 2.*Bd(i-1,:) + 2.*r.*Bd1(i-1,)-Bd1(i-2,:);
end
Bd2 = zeros(2*m-1,m);
Bd2(1:2,:) = zeros(2,m);
for i = 3:m
    Bd2(i,:) = 4.*Bd1(i-1,)+2.*r.*Bd2(i-1,)-Bd2(i-2,:);
end
B = Bd(1:m,:); %B matrix
B1 = Bd1(1:m,:);
B2 = Bd2(1:m,:);
for i = 1:m
    Bd2(:,i) = -2.*Bd(:,i) -4.*r(i).*Bd1(:,i) + (1-r(i).^2).*Bd2(:,i);
end
for i = 1:m
    Bd1(:,i) = -2.*r(i).*Bd(:,i) + (1-r(i).^2).*Bd1(:,i);
end
for i = 1:m
    Bd(:,i) = (1-r(i).^2).*Bd(:,i);
end
Bz = zeros(m); %B matrix for z
B1z = zeros(m);
B2z = zeros(m);
for i = 1:m
    Bz(i,:) = Bd(2*i-1,:);
    B1z(i,:) = Bd1(2*i-1,:);
    B2z(i,:) = Bd2(2*i-1,:);
end
%%%%%%%%%%%%%%%%%%%%%%%%%%%%%%%%%%%%%%%%%%%%%%%%%%%%%%%%%%%%%%%%%%%%%%%%

%Parameters for Newton's method
%%%%%%%%%%%%%%%%%%%%%%%%%%%%%%%%%%%%%%%%%%%%%%%%%%%%%%%%%%%%%%%%%%%%%%%%
N_max = 100; %Maximum iterations Newton's method
tolerance = 10^(-10); %Tolerance Newton's method
%%%%%%%%%%%%%%%%%%%%%%%%%%%%%%%%%%%%%%%%%%%%%%%%%%%%%%%%%%%%%%%%%%%%%%%%

%Newton's method pulsating flow (actual calculation)
%%%%%%%%%%%%%%%%%%%%%%%%%%%%%%%%%%%%%%%%%%%%%%%%%%%%%%%%%%%%%%%%%%%%%%%%
dpdz = pbar.*amplitude.*(1+sin(t)); %pulsating pressure gradient
x_init = ones(totalv,1); %initial conditions
tic %start timer
for tm = 0:0.2:0.2 %0th order continuation,
    %change continuation parameter if necessary
    %additional model parameters grouped together in a single vector for
    %convenience
    arguments = [tm kc kd p eta0 G tr tl tlambda ta tb];
    x_sol = NewtonTVDV14(equations,Jacobian,x_init,N_max,tolerance,n,m,...
        totalv,dpdz,A,A1,A2,Az,A1z,B,B1,B2,Bz,B1z,B2z,Wo,r,arguments);
    x_init = x_sol;
end

```

```

end
time1 = toc; %time how long Newton's method takes
%%%%%%%%%%%%%%%%%%%%%%%%%%%%%%%%%%%%%%%%%%%%%%%%%%%%%%%%%%%%%%%%%%%%%%%%

%Translate back to outputvariables
%%%%%%%%%%%%%%%%%%%%%%%%%%%%%%%%%%%%%%%%%%%%%%%%%%%%%%%%%%%%%%%%%%%%%%%%
Z = zeros(2*n+1,m); %Initiate matrices
Taul2 = zeros(2*n+1,m);
% Lambda = zeros(2*n+1,m);
%Add more output variables if needed
for i=1:2*n+1
    for j = 1:m
        Z(i,j) = x_sol(j+(i-1)*m);
        Taul2(i,j) = x_sol((2*n+1)*m+j+(i-1)*m);
        % Lambda(i,j) = x_sol(2*(2*n+1)*m+j+(i-1)*m);
    end
end
%%%%%%%%%%%%%%%%%%%%%%%%%%%%%%%%%%%%%%%%%%%%%%%%%%%%%%%%%%%%%%%%%%%%%%%%

%Newton's method steady state solution
%%%%%%%%%%%%%%%%%%%%%%%%%%%%%%%%%%%%%%%%%%%%%%%%%%%%%%%%%%%%%%%%%%%%%%%%
dpdz = pbar.*amplitude.*ones(length(t),1); %steady state pressure gradient
x_init = ones(totalv,1); %initial conditions
tic
for tm = 0:0.2:0.2
    arguments = [tm kc kd p eta0 G tr t1 tlambda ta tb];
    x_sol = NewtonTVDV14(equations,Jacobian,x_init,N_max,tolerance,n,m,...
        totalv,dpdz,A,A1,A2,Az,Alz,B,B1,B2,Bz,B1z,B2z,Wo,r,arguments);
    x_init = x_sol;
end
time2 = toc;

%Translate back to outputvariables
%%%%%%%%%%%%%%%%%%%%%%%%%%%%%%%%%%%%%%%%%%%%%%%%%%%%%%%%%%%%%%%%%%%%%%%%
Z_SS = zeros(2*n+1,m);
Taul2_SS = zeros(2*n+1,m);
% Lambda_SS = zeros(2*n+1,m);
%Add more output variables if needed
for i=1:2*n+1
    for j = 1:m
        Z_SS(i,j) = x_sol(j+(i-1)*m);
        Taul2_SS(i,j) = x_sol((2*n+1)*m+j+(i-1)*m);
        % Lambda_SS(i,j) = x_sol(2*(2*n+1)*m+j+(i-1)*m);
    end
end
%%%%%%%%%%%%%%%%%%%%%%%%%%%%%%%%%%%%%%%%%%%%%%%%%%%%%%%%%%%%%%%%%%%%%%%%

%difference between pulsating and steady state part (oscillating part)
%%%%%%%%%%%%%%%%%%%%%%%%%%%%%%%%%%%%%%%%%%%%%%%%%%%%%%%%%%%%%%%%%%%%%%%%
Z_o = Z - Z_SS;
Taul2_o = Taul2 - Taul2_SS;
% Lambda_o = Lambda - Lambda_SS;
%%%%%%%%%%%%%%%%%%%%%%%%%%%%%%%%%%%%%%%%%%%%%%%%%%%%%%%%%%%%%%%%%%%%%%%%

%Make matrices A and B again with more points to plot
%%%%%%%%%%%%%%%%%%%%%%%%%%%%%%%%%%%%%%%%%%%%%%%%%%%%%%%%%%%%%%%%%%%%%%%%
tpoints = 90; %number of discrete time points for plotting
rpoints = 101; %number of discrete radial points for plotting
t = linspace(0,T,tpoints)';

```

```

r = linspace(0,1,rpoints);
A = zeros(tpoints,2*n+1);
A(:,1) = ones(tpoints,1);
j = 1;
for i = 2:2:2*n+1
    A(:,i) = sin(j.*t);
    j = j+1;
end
j = 1;
for i = 3:2:2*n+1
    A(:,i) = cos(j.*t);
    j = j + 1;
end

A1 = zeros(tpoints,2*n+1);
A1(:,1) = zeros(tpoints,1);
j = 1;
for i = 2:2:2*n+1
    A1(:,i) = j.*cos(j.*t);
    j = j+1;
end
j = 1;
for i = 3:2:2*n+1
    A1(:,i) = -j.*sin(j.*t);
    j = j + 1;
end

Az = A;
Az(:,1) = t;
A1z = A1;
A1z(:,1) = ones(tpoints,1);
Bd = zeros(2*m-1,rpoints);
Bd(1,:) = ones(1,rpoints);
Bd(2,:) = r;
for i = 3:2*m-1
    Bd(i,:) = 2.*r.*Bd(i-1,:)-Bd(i-2,:);
end
Bd1 = zeros(2*m-1,rpoints);
Bd1(1,:) = zeros(1,rpoints);
Bd1(2,:) = ones(1,rpoints);
for i = 3:2*m-1
    Bd1(i,:) = 2.*Bd(i-1,:) + 2.*r.*Bd1(i-1,:)-Bd1(i-2,:);
end
B = Bd(1:m,:);
B1 = Bd1(1:m,:);
for i = 1:rpoints
    Bd1(:,i) = -2.*r(i).*Bd(:,i) + (1-r(i).^2).*Bd1(:,i);
end
for i = 1:rpoints
    Bd(:,i) = (1-r(i).^2).*Bd(:,i);
end
Bz = zeros(m,rpoints);
Blz = zeros(m,rpoints);
for i = 1:m
    Bz(i,:) = Bd(2*i-1,:);
    Blz(i,:) = Bd1(2*i-1,:);
end
%%%%%%%%%%%%%%%%%%%%%%%%%%%%%%%%%%%%%%%%%%%%%%%%%%%%%%%%%%%%%%%%%%%%%%%%%%
%Construct output variables

```

```

%%%%%%%%%%%%%%%%%%%%%%%%%%%%%%%%%%%%%%%%%%%%%%%%%%%%%%%%%%%%%%%%%%%%%%%%
vz = (A1z*Z*Bz);
% gamma_o = Az*Z_o*B1z;
% gammadot_o = omega.*(A1z*Z_o*B1z);
% tau12n_o = eta*gammadot_o; %Shear stress for Newtonian fluid
% tau12p = eta*(1 + (eta0-1).*(1+gammadot.^2).^((p-1)./2)).*gammadot;
% Shear stress for carreau fluid
tau12_o = eta.*omega.*(A*Tau12_o*B);
% lambda = A*Lambda*B;
%%%%%%%%%%%%%%%%%%%%%%%%%%%%%%%%%%%%%%%%%%%%%%%%%%%%%%%%%%%%%%%%%%%%%%%%

%Plot variables
%%%%%%%%%%%%%%%%%%%%%%%%%%%%%%%%%%%%%%%%%%%%%%%%%%%%%%%%%%%%%%%%%%%%%%%%

%%%%%%%%%%%%%%%%%%%%%%%%%%%%%%%%%%%%%%%%%%%%%%%%%%%%%%%%%%%%%%%%%%%%%%%%

```

```

function [x_sol, iterations] = NewtonTVDV14(equations, Jacobian, x_init, ...
    N_max, tolerance, n, m, totalv, dpdz, A, A1, A2, Az, Alz, B, B1, B2, Bz, Blz, B2z, Wo...
    , r, arguments)
% Newtonp implements Newton's iterative method for the solution of fp(x,p)=0
% INPUT:
% fp: user supplied function of y,p function the root(s) of which are sought
% fpdy: user supplied function of y,p the derivative of fp wrt y
% x: is the independent variable (=y)
% x_init: is the initial guess for the independent variable
% N_max: is the maximum number of iterations (10 recommended)
% tolerance: is the absolute tolerance for the solution
% WARNING When called with external functions, the function handles (@)
% should precede fp and fpdy : ... Newtonp(@fp,@fpdy,...
% OUTPUT:
% x_sol: is the solution (if converged) or last guess (if not converged)
% iterations: number of iterations (k) required for convergence within
% given tolerance;
% is equal to -(N_max+1) if no solution is found within N_max iterations;
% it takes a negative value -k if the procedure diverged after k iterations
iterations = 0;
x_sol = x_init;
diff = Jacobian(equations, x_sol, n, m, totalv, dpdz, A, A1, A2, Az, Alz, B, B1, B2, Bz...
    , Blz, B2z, Wo, r, arguments) \ equations(x_sol, n, m, totalv, dpdz, A, A1, A2, Az, ...
    Alz, B, B1, B2, Bz, Blz, B2z, Wo, r, arguments);
diff_mag_old = norm(diff);
x_sol = x_sol - diff;

for k=1:N_max
    diff = Jacobian(equations, x_sol, n, m, totalv, dpdz, A, A1, A2, Az, Alz, B, B1, B2...
        , Bz, Blz, B2z, Wo, r, arguments) \ equations(x_sol, n, m, totalv, dpdz, A, A1, ...
        A2, Az, Alz, B, B1, B2, Bz, Blz, B2z, Wo, r, arguments);
    diff_mag = norm(diff);
    if(diff_mag < tolerance)
        iterations = k;
        x_sol = x_sol - diff;
        break
    elseif(diff_mag > 1000*diff_mag_old)
        iterations = -k;
        disp('Warning! Algorithm diverged!')
        break
    end
    diff_mag_old=diff_mag;
    x_sol = x_sol - diff;
end
if(iterations == 0)
    iterations = -(N_max+1);
    disp('Warning! There is no convergence within N_max iterations')
end
end

```

```

function J = dfdxTVDV14(equations,var,n,m,totalv,dpdz,A,A1,A2,Az,A1z,B,...
    B1,B2,Bz,B1z,B2z,Wo,r,arguments)
%Jacobian
%Find Jacobian in numerical way
a = 10^(-6);
F = equations(var,n,m,totalv,dpdz,A,A1,A2,Az,A1z,B,B1,B2,Bz,B1z,B2z,Wo,...
    r,arguments);
J = zeros(totalv);
I = eye(totalv);
for i = 1:totalv
    for j = 1:totalv
        Fi = equations(var+a*I(:,j),n,m,totalv,dpdz,A,A1,A2,Az,A1z,B,B1,...
            B2,Bz,B1z,B2z,Wo,r,arguments);
        J(i,j) = (Fi(i)-F(i))/a;
    end
end
end
end

```

```

function F = ftVDV14N(var,n,m,totalv,dpdz,A,A1,A2,Az,Alz,B,B1,B2,Bz,Blz,B2z,Wo,r,
arguments)
%Newtonian fluid
%Inititalize matrices
%%%%%%%%%%%%%%%%%%%%%%%%%%%%%%%%%%%%%%%%%%%%%%%%%%%%%%%%%%%%%%%%%%%%%%%%
Z = zeros(2*n+1,m);
Lambda = zeros(2*n+1,m);
F = zeros(totalv,1);
for i = 1:2*n+1
    for j = 1:m
        Z(i,j) = var(j+(i-1)*m);
        Lambda(i,j) = var((2*n+1)*m+j+(i-1)*m);
    end
end
%%%%%%%%%%%%%%%%%%%%%%%%%%%%%%%%%%%%%%%%%%%%%%%%%%%%%%%%%%%%%%%%%%%%%%%%

%equations (Cauchy momentum + stress + structural)
%evaluated at the different radial and time points
%%%%%%%%%%%%%%%%%%%%%%%%%%%%%%%%%%%%%%%%%%%%%%%%%%%%%%%%%%%%%%%%%%%%%%%%
tau = Alz*Z*B1z;
dtaudr = (Alz*Z*B2z);
dvdt = A2*Z*Bz;
lambda = A*Lambda*B;
dlambdadt = A1*Lambda*B;
gammadot = Alz*Z*B1z;
for i = 1:2*n+1
    for j = 1:m
        F(j+(i-1)*m) = r(j)*Wo^2*dvdt(i,j) + r(j)*dpdz(i) - (tau(i,j) + ...
            r(j)*dtaudr(i,j));
        F((2*n+1)*m+j+(i-1)*m) = arguments(9)*dlambdadt(i,j) - ...
            ((1-lambda(i,j))+(1-lambda(i,j))*arguments(10)*...
            abs(gammadot(i,j))-lambda(i,j)*...
            (arguments(11)*gammadot(i,j))^2);
    end
end
%%%%%%%%%%%%%%%%%%%%%%%%%%%%%%%%%%%%%%%%%%%%%%%%%%%%%%%%%%%%%%%%%%%%%%%%

```

```

function F = ftVDV14M(var,n,m,totalv,dpdz,A,A1,A2,Az,A1z,B,B1,B2,Bz,B1z,B2z,Wo,r,
arguments)
%Maxwell fluid
%Inititalize matrices
%%%%%%%%%%%%%%%%%%%%%%%%%%%%%%%%%%%%%%%%%%%%%%%%%%%%%%%%%%%%%%%%%%%%%%%%
Z = zeros(2*n+1,m);
Tau = zeros(2*n+1,m);
F = zeros(totalv,1);
for i = 1:2*n+1
    for j = 1:m
        Z(i,j) = var(j+(i-1)*m);
    end
end
for i = 1:2*n+1
    for j = 1:m
        Tau(i,j) = var((2*n+1)*m+j+(i-1)*m);
    end
end
%%%%%%%%%%%%%%%%%%%%%%%%%%%%%%%%%%%%%%%%%%%%%%%%%%%%%%%%%%%%%%%%%%%%%%%%

%equations (Cauchy momentum + stress + structural)
%%%%%%%%%%%%%%%%%%%%%%%%%%%%%%%%%%%%%%%%%%%%%%%%%%%%%%%%%%%%%%%%%%%%%%%%
tau = A*Tau*B;
dtaudr = A*Tau*B1;
dtaudt = A1*Tau*B;
gammadot = A1z*Z*B1z;
dvdt = A2*Z*Bz;
for i = 1:2*n+1
    for j = 1:m
        F(j+(i-1)*m) = r(j)*Wo^2*dvdt(i,j) + r(j)*dpdz(i) - (tau(i,j) ...
            + r(j)*dtaudr(i,j));
        F((2*n+1)*m+j+(i-1)*m) = arguments(1)*dtaudt(i,j) + tau(i,j) - ...
            gammadot(i,j);
    end
end
%%%%%%%%%%%%%%%%%%%%%%%%%%%%%%%%%%%%%%%%%%%%%%%%%%%%%%%%%%%%%%%%%%%%%%%%

```

```

function F = fTVDV14P(var,n,m,totalv,dpdz,A,A1,A2,Az,Alz,B,B1,B2,Bz,B1z,...
    B2z,Wo,r,arguments)
%Carreau model
%Inititalize matrices
%%%%%%%%%%%%%%%%%%%%%%%%%%%%%%%%%%%%%%%%%%%%%%%%%%%%%%%%%%%%%%%%%%%%%%%%
Z = zeros(2*n+1,m);
F = zeros(totalv,1);
for i = 1:2*n+1
    for j = 1:m
        Z(i,j) = var(j+(i-1)*m);
    end
end
%%%%%%%%%%%%%%%%%%%%%%%%%%%%%%%%%%%%%%%%%%%%%%%%%%%%%%%%%%%%%%%%%%%%%%%%

%equations (Cauchy momentum + stress + structural)
%%%%%%%%%%%%%%%%%%%%%%%%%%%%%%%%%%%%%%%%%%%%%%%%%%%%%%%%%%%%%%%%%%%%%%%%
dvdtdt = A2*Z*Bz;
gammadot = Alz*Z*B1z;
dgammadotdr = Alz*Z*B2z;
visc = 1 + (arguments(5)-1).*(1+gammadot.^2).^(arguments(4)-1)./2);
dviscdr = (arguments(4)-1).*(arguments(5)-1).*gammadot.*(gammadot.^2+1)...
    .^(arguments(4)-3)/2).*dgammadotdr;
tau = visc.*gammadot;
dtaudr = dviscdr.*gammadot + visc.*dgammadotdr;
for i = 1:2*n+1
    for j = 1:m
        F(j+(i-1)*m) = r(j)*Wo^2*dvdtdt(i,j) + r(j)*dpdz(i) - (tau(i,j) + ...
            r(j)*dtaudr(i,j));
    end
end
%%%%%%%%%%%%%%%%%%%%%%%%%%%%%%%%%%%%%%%%%%%%%%%%%%%%%%%%%%%%%%%%%%%%%%%%

```

```

function F = ftVDV14S3 (var,n,m,totalv,dpdz,A,A1,A2,Az,A1z,B,B1,B2,Bz,B1z,...
    B2z,Wo,r,arguments)
%Stephanou model
%Initialize matrices
%%%%%%%%%%%%%%%%%%%%%%%%%%%%%%%%%%%%%%%%%%%%%%%%%%%%%%%%%%%%%%%%%%%%%%%%
Z = zeros(2*n+1,m);
% C12 = zeros(2*n+1,m);
Taul2 = zeros(2*n+1,m);
Lambda = zeros(2*n+1,m);
F = zeros(totalv,1);
for i=1:2*n+1
    for j = 1:m
        Z(i,j) = var(j+(i-1)*m);
%         C12(i,j) = var((2*n+1)*m+j+(i-1)*m);
        Taul2(i,j) = var((2*n+1)*m+j+(i-1)*m);
        Lambda(i,j) = var(2*(2*n+1)*m+j+(i-1)*m);
    end
end

%%%%%%%%%%%%%%%%%%%%%%%%%%%%%%%%%%%%%%%%%%%%%%%%%%%%%%%%%%%%%%%%%%%%%%%%

%equations (Cauchy momentum + stress + structural)
%%%%%%%%%%%%%%%%%%%%%%%%%%%%%%%%%%%%%%%%%%%%%%%%%%%%%%%%%%%%%%%%%%%%%%%%
% c12 = A*C12*B;
% dc12dt = A1*C12*B;
taul2 = A*Taul2*B;
dtaul2dt = A1*Taul2*B;
dtaul2dr = A*Taul2*B1;
gammadot = A1z*Z*B1z;
dvdt = A2*Z*Bz;
lambda = A*Lambda*B;
dlambdadt = A1*Lambda*B;

for i = 1:2*n+1
    for j = 1:m
        F(j+(i-1)*m) = r(j)*Wo^2*dvdt(i,j) + r(j)*dpdz(i) - (taul2(i,j)...
            + r(j)*dtaul2dr(i,j));
        F((2*n+1)*m+j+(i-1)*m) = taul2(i,j) - arguments(6)*...
            (-dtaul2dt(i,j)*arguments(7)/(1-lambda(i,j)) + 0.5*...
            lambda(i,j)*(lambda(i,j)-1-(lambda(i,j)-1)^2/2)*...
            dtaul2dt(i,j)*arguments(7)/(1-lambda(i,j))) - gammadot(i,j);
        F(2*(2*n+1)*m+j+(i-1)*m) = arguments(9)*dlambdadt(i,j) - ...
            ((1-lambda(i,j))*(100+30*abs(gammadot(i,j))) - ...
            gammadot(i,j)^2*lambda(i,j));
    end
end

%%%%%%%%%%%%%%%%%%%%%%%%%%%%%%%%%%%%%%%%%%%%%%%%%%%%%%%%%%%%%%%%%%%%%%%%

```

```
function x = chebyshev_coefficients ( a, b, n )

    angle = ( 1 : 2 : ( 2 * n - 1 ) ) * pi / ( 2 * n );
    angle = angle';
    x = -cos ( angle );
    x = 0.5 * ( a + b ) + x * 0.5 * ( b - a );

end
```

Appendix E
SOFTWARE LICENSE FILES

This appendix includes proof that the author has the right to use the software package MATLAB from Mathworks.



MathWorks Account

My Software

	License	Label	Option	Use			
Tim Van de Vy... (timvandeVyver)	919019	Individual	Total Headcount	Academic			

[MATLAB Drive](#)

[MATLAB Online](#)

[Self-Paced Courses](#)

[Service Requests](#)

[Bug Reports](#)

[Online Services Agreement](#)

Hardware Support

Connect to hardware platforms like Arduino and Raspberry Pi.

[Learn more](#)

[+ Associate to an additional license](#)

[+ Get a trial](#)

[mathworks.com](#)

© 1994-2019 The MathWorks, Inc. MATLAB and Simulink are registered trademarks of The MathWorks, Inc. See [mathworks.com/trademarks](#) for a list of additional trademarks. Other product or brand names may be trademarks or registered trademarks of their respective holders.



License Center

License: 919019

Individual

Use-Option: Academic - Total Headcount

Master License: 30919019

Term: Annual

MATLAB Online: [Access Now](#)


Manage Products

Install and Activate

Contact Administrator(s)

Download

Product	Service End Date	Count
Standard Suite	31 Oct 2019	1
Aerospace Blockset	31 Oct 2019	1
Aerospace Toolbox	31 Oct 2019	1
Audio Toolbox	31 Oct 2019	1
Communications Toolbox	31 Oct 2019	1
Computer Vision Toolbox	31 Oct 2019	1
Database Toolbox	31 Oct 2019	1
Datafeed Toolbox	31 Oct 2019	1
Deep Learning Toolbox	31 Oct 2019	1
Econometrics Toolbox	31 Oct 2019	1
Embedded Coder	31 Oct 2019	1
Financial Instruments Toolbox	31 Oct 2019	1
Financial Toolbox	31 Oct 2019	1
Fixed-Point Designer	31 Oct 2019	1
Fuzzy Logic Toolbox	31 Oct 2019	1
Global Optimization Toolbox	31 Oct 2019	1
HDL Coder	31 Oct 2019	1
Image Acquisition Toolbox	31 Oct 2019	1
MATLAB Coder	31 Oct 2019	1
MATLAB Compiler	31 Oct 2019	1
MATLAB Compiler SDK	31 Oct 2019	1
MATLAB Report Generator	31 Oct 2019	1

Product	Service End Date	Count
Mapping Toolbox	31 Oct 2019	1
Model Predictive Control Toolbox	31 Oct 2019	1
Partial Differential Equation Toolbox	31 Oct 2019	1
Phased Array System Toolbox	31 Oct 2019	1
RF Toolbox	31 Oct 2019	1
Robotics System Toolbox	31 Oct 2019	1
Robust Control Toolbox	31 Oct 2019	1
SimBiology	31 Oct 2019	1
SimEvents	31 Oct 2019	1
Simscape Driveline	31 Oct 2019	1
Simscape Electrical	31 Oct 2019	1
 Simscape Electronics (Transitioned)	31 Oct 2019	1
Simscape Fluids	31 Oct 2019	1
Simulink 3D Animation	31 Oct 2019	1
Simulink Check	31 Oct 2019	1
Simulink Coder	31 Oct 2019	1
Simulink Coverage	31 Oct 2019	1
Simulink Design Optimization	31 Oct 2019	1
Simulink Desktop Real-Time	31 Oct 2019	1
Simulink PLC Coder	31 Oct 2019	1
Simulink Real-Time	31 Oct 2019	1
Simulink Report Generator	31 Oct 2019	1
Simulink Requirements	31 Oct 2019	1
Spreadsheet Link	31 Oct 2019	1
System Identification Toolbox	31 Oct 2019	1
Text Analytics Toolbox	31 Oct 2019	1
Vehicle Network Toolbox	31 Oct 2019	1
Wavelet Toolbox	31 Oct 2019	1

[mathworks.com](https://www.mathworks.com)

© 1994-2019 The MathWorks, Inc. MATLAB and Simulink are registered trademarks of The MathWorks, Inc. See [mathworks.com/trademarks](https://www.mathworks.com/trademarks) for a list of additional trademarks. Other product or brand names may be trademarks or registered trademarks of their respective holders.